

Stress dynamically modulates neuronal autophagy to gate depression onset

<https://doi.org/10.1038/s41586-025-08807-4>

Received: 24 July 2023

Accepted: 19 February 2025

Published online: 9 April 2025

Open access

 Check for updates

Liang Yang^{1,2,3,13}, Chen Guo^{1,2,3,13}, Zhiwei Zheng^{1,2,3,13}, Yiyang Dong^{1,4,5,13}, Qifeng Xie^{1,2,3}, Zijian Lv^{1,2,3}, Min Li^{1,4,5}, Yangyang Lu^{6,7}, Xiaonan Guo^{1,4,5}, Rongshan Deng^{1,4,5}, Yiqin Liu^{1,2,3}, Yirong Feng^{1,4,5}, Ruiqi Mu^{1,2,3}, Xuliang Zhang⁸, Huan Ma^{2,3}, Zhong Chen⁹, Zhijun Zhang^{10,11}, Zhaoqi Dong¹², Wei Yang⁵, Xiangnan Zhang^{6,7}✉ & Yihui Cui^{1,2,3}✉

Chronic stress remodels brain homeostasis, in which persistent change leads to depressive disorders¹. As a key modulator of brain homeostasis², it remains elusive whether and how brain autophagy is engaged in stress dynamics. Here we discover that acute stress activates, whereas chronic stress suppresses, autophagy mainly in the lateral habenula (LHb). Systemic administration of distinct antidepressant drugs similarly restores autophagy function in the LHb, suggesting LHb autophagy as a common antidepressant target. Genetic ablation of LHb neuronal autophagy promotes stress susceptibility, whereas enhancing LHb autophagy exerts rapid antidepressant-like effects. LHb autophagy controls neuronal excitability, synaptic transmission and plasticity by means of on-demand degradation of glutamate receptors. Collectively, this study shows a causal role of LHb autophagy in maintaining emotional homeostasis against stress. Disrupted LHb autophagy is implicated in the maladaptation to chronic stress, and its reversal by autophagy enhancers provides a new antidepressant strategy.

Major depressive disorder is one of the most disabling psychiatric disorders, with a global lifetime prevalence of 10.6% (ref. 3). Stress is a significant risk factor for depression and widely present in daily life. Moderate stress in the short term is beneficial for survival, whereas prolonged stress exposure can perturb emotional homeostasis and contribute to depression¹. However, it remains elusive how the brain dynamically copes with stress. Understanding the dynamic cellular mechanisms within specific neural circuits underlying stress is crucial for the development of more efficacious antidepressant treatments.

Protein turnover by degradation and synthesis allows fine-tuning of neuronal homeostasis⁴. Among various mechanisms that control protein turnover, autophagy (herein mainly concerning macroautophagy) has drawn increasing attention in recent decades². Autophagy is a major catabolic stepwise process through which intracellular proteins are engulfed in autophagosomes and subsequently transported to lysosomes for degradation⁵. Notably, though autophagy genes are extensively expressed in the nervous system, the physiological function of brain autophagy remains an open question. So far most research has focused on its role in neurological diseases^{2,5-7}, leaving an enormous opportunity for exploring its role in stress-related psychiatric diseases.

By specifically targeting the degradation of synaptic components⁸⁻¹⁴, brain autophagy has been suggested to regulate synaptic function and

various related physio- and pathological functions, including learning and memory¹⁵⁻¹⁸ and psychiatric disorders¹⁹⁻²⁵. Yet, little has been uncovered regarding the precise cellular substrates and neural circuits underlying how brain autophagy regulates emotions during stress.

The clinical relevance of autophagy dysfunction in depression has been demonstrated by impaired autophagy-related signalling (for example, mTOR, p62, LC3, Atg7, Beclin-1) in blood or brain samples from patients with depression²³. Conversely, autophagy signalling is elevated in samples from patients with depression and stressed animals treated with antidepressants^{24,26}. Nevertheless, the precise targets to which antidepressants regulate autophagy in the brain remain elusive.

The lateral habenula (LHb), one of the most vulnerable targets of stress, is extensively activated by numerous stressors²⁷⁻³² and therefore shows a high turnover of synaptic proteins^{30,33}. In particular, chronic stress potentiates excitatory inputs, alters the expression of various synaptic proteins and disrupts neuronal homeostasis in the LHb²⁷⁻³². Here we found that LHb autophagy is essential for emotional homeostasis through counterbalancing excessive synaptic proteins upregulated by stress. We discovered a causal role of LHb autophagy in coping with stress. Maladaptation to chronic stress disrupts LHb autophagy, the reversal of which provides exciting possibilities for new rapid and sustained antidepressant strategies.

¹Department of Psychiatry of Sir Run Run Shaw Hospital and School of Brain Science and Brain Medicine, Zhejiang University School of Medicine, Hangzhou, China. ²MOE Frontier Science Center for Brain Science and Brain-Machine Integration, Zhejiang University, Hangzhou, China. ³NHC and CAMS Key Laboratory of Medical Neurobiology, Zhejiang University, Hangzhou, China. ⁴International Institutes of Medicine, The Fourth Affiliated Hospital of Zhejiang University School of Medicine, Yiwu, China. ⁵Department of Biophysics and Department of Neurology of the Fourth Affiliated Hospital, Zhejiang University School of Medicine, Hangzhou, China. ⁶Institute of Pharmacology and Toxicology, College of Pharmaceutical Sciences, State Key Laboratory of Advanced Drug Delivery and Release Systems, Zhejiang University, Hangzhou, China. ⁷Jinhua Institute of Zhejiang University, Jinhua, China. ⁸Laboratory Animal Center, Zhejiang University, Hangzhou, China. ⁹Zhejiang Key Laboratory of Neuropsychopharmacology, Zhejiang Chinese Medical University, Hangzhou, China. ¹⁰Department of Neurology, Affiliated Zhongda Hospital, School of Medicine, Institute of Neuropsychiatry, Key Laboratory of Developmental Genes and Human Disease, Southeast University, Nanjing, China. ¹¹Department of Mental Health and Public Health, Faculty of Life and Health Sciences, Shenzhen Institute of Advanced Technology, Chinese Academy of Sciences, Shenzhen, China. ¹²Department of Neurobiology, School of Basic Medical Sciences, Capital Medical University, Beijing, China. ¹³These authors contributed equally: Liang Yang, Chen Guo, Zhiwei Zheng, Yiyang Dong. ✉e-mail: xiangnan_zhang@zju.edu.cn; yihucui@zju.edu.cn

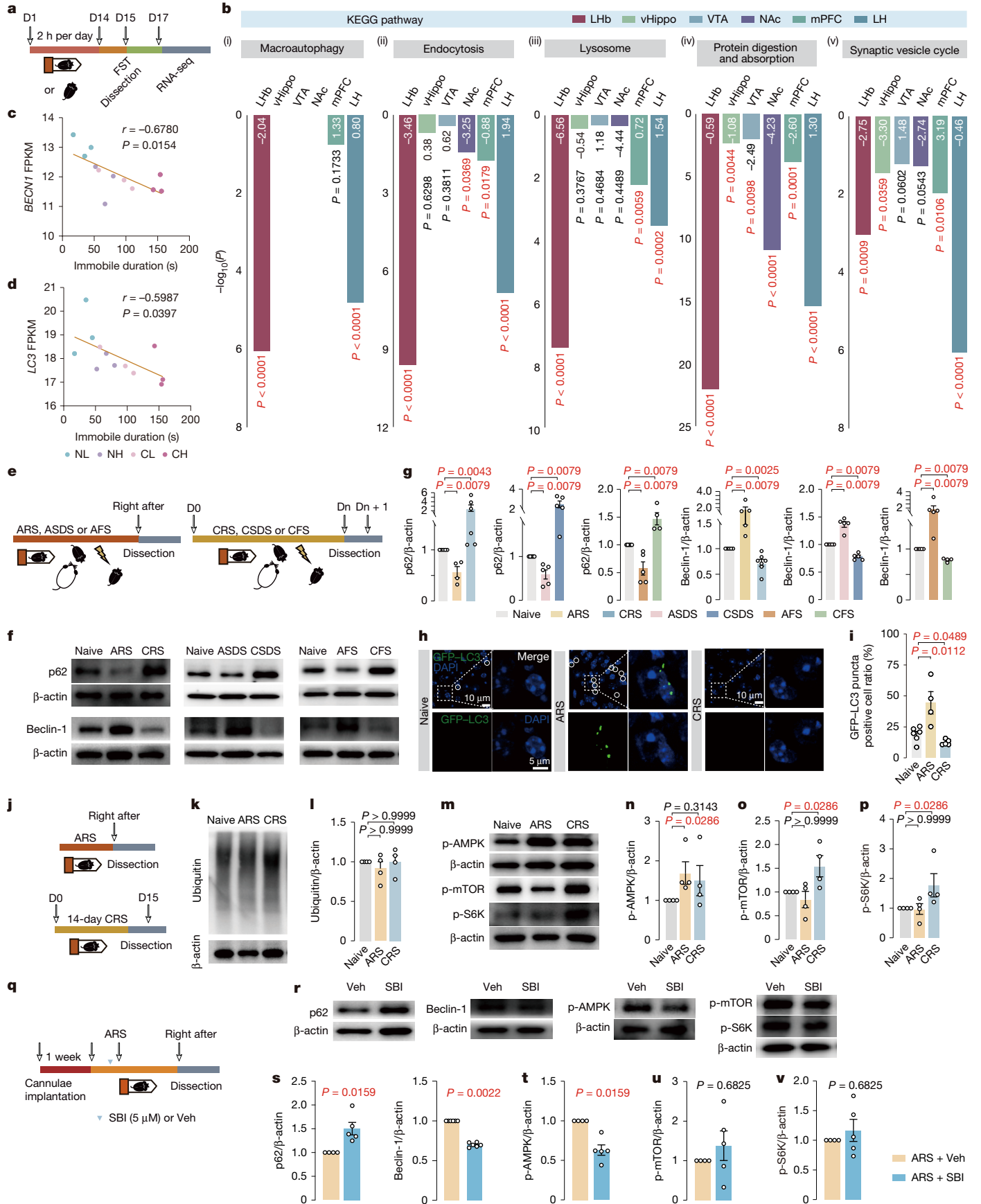


Fig. 1 | See next page for caption.

Fig. 1 | Acute stress activates, whereas chronic stress impairs, Lhb autophagy. **a**, Experimental design. D, day. **b**, Two-sided classic KEGG analysis of bulk RNA-seq ($n_{\text{naive/CRS}} = 3$ per group; numbers on the bar indicate the corresponding z -score). LH, lateral hypothalamus. **c, d**, Correlation of *Becn1* (**c**) and *LC3* (**d**) mRNA fragments per kilobase million (FPKM) with behavioural scores ($n = 12$ mice). CH, CRS mice with high FST; CL, CRS mice with low FST; NH, naive mice with high FST; NL, naive mice with low FST. **e**, Experimental designs. AFS, acute footshock stress; ASDS, acute social defeat stress; CFS, chronic footshock stress; CSDS, chronic social defeat stress. **f, g**, Representative images (**f**) and quantification (**g**) of western blot (p62, $n_{\text{naive/ARS/CRS}} = 5, 4, 6$; Beclin-1, $n_{\text{naive/ARS/CRS}} = 5, 5, 7$; $n_{\text{naive/ASDS/CSDS}} = 5$ per group for p62 and Beclin-1; $n_{\text{naive/AFS/CFS}} = 5, 5, 4$ for p62 and Beclin-1). **h, i**, Representative images (**h**) and quantification (**i**)

of the proportion of GFP-puncta-positive cells in Lhb of GFP-LC3 mice treated with ARS and CRS. White circles denote colocalization of GFP-LC3 puncta and DAPI ($n_{\text{naive/ARS/CRS}} = 6/4/5$). **j**, Experimental designs. **k–p**, Representative images (**k, m**) and quantification of ubiquitin (**l**), p-AMPK (**n**), p-mTOR (**o**) and p-S6K (**p**) western blot ($n_{\text{naive/ARS/CRS}} = 4$ per group). **q–v**, Experimental design (**q**), representative images (**r**) and quantification of p62 and Beclin-1 (**s**, p62, $n_{\text{ARS+Veh/CRS+SBI}} = 4, 5$; Beclin-1, $n_{\text{ARS+Veh/CRS+SBI}} = 6$ per group), p-AMPK (**t**, $n_{\text{ARS+Veh/CRS+SBI}} = 4, 5$), p-mTOR (**u**, $n_{\text{ARS+Veh/CRS+SBI}} = 4, 5$) and p-S6K (**v**, $n_{\text{ARS+Veh/CRS+SBI}} = 4, 5$) western blot showing effect of SBI treatment on autophagy. Veh, vehicle. Two-sided Mann–Whitney test (**g, l, m–p, s–v**), two-sided unpaired t -test (**i**) and Pearson correlation test (**c, d**). Data are mean \pm s.e.m. Schematics in **a, e, j, k** adapted from ref. 31, Elsevier.

Antidepressants activate Lhb autophagy

Given the potential role of autophagy in the actions of antidepressant drugs²⁴, we evaluated whether autophagy levels in specialized brain circuits were modulated by antidepressants in mice that received chronic restraint stress (CRS), a well-established animal model of depression^{29,31}. We measured in parallel autophagy levels in nine stress-related brain regions under the systemic administration of either a classical selective serotonin reuptake inhibitor (SSRI) paroxetine³⁴ or a new rapid antidepressant ketamine³⁵ (Extended Data Fig. 1a,b). We observed that both paroxetine (Extended Data Fig. 1a) and ketamine (Extended Data Fig. 1b) enhanced autophagy in the Lhb. This was demonstrated by decreased protein level of p62 (Extended Data Fig. 1a1,b1), a classical autophagy marker degraded by autophagic processes², and increased protein level of Beclin-1 (Extended Data Fig. 1a2,b2), which is specifically involved in autophagosome formation². Meanwhile, p62 and Beclin-1 levels in eight other brain regions were unaffected by either paroxetine or ketamine, including the ventral hippocampus (vHippo), medial prefrontal cortex (mPFC), ventral tegmental areas (VTA), lateral hypothalamus, nucleus accumbens (NAc), lateral septum, dorsal raphe nucleus and median raphe nucleus (Extended Data Fig. 1a,b), suggesting that regulatory effects of distinct antidepressants on brain autophagy take place mainly in the Lhb. One day of treatment of paroxetine had no impact on depression-like behaviours (Extended Data Fig. 2a,b) and did not alter p62 or Beclin-1 levels in the Lhb (Extended Data Fig. 2c). In parallel, 7 days, but not 1 day, of treatment of paroxetine significantly reduced excitatory synaptic transmission and bursting activity in Lhb neurons of CRS mice (Extended Data Fig. 2d–i). These results indicate that activation of Lhb autophagy is temporally coincided with the silencing of Lhb neuronal activity and the onset of paroxetine's antidepressant-like effects in chronic stressed mice³⁴.

CRS impairs Lhb autophagy

To further investigate the clinical relevance of Lhb autophagy in depression, we analysed in parallel autophagy-related gene expression levels by bulk RNA sequencing (RNA-seq) in six emotion-related brain regions. Transcriptomic profiles were compared between naive and CRS mice after completing a depression-like behavioural test, the forced swim test (FST) (Fig. 1a). Using KEGG (Kyoto Encyclopedia of Genes and Genomes) enrichment analysis, we found that genes engaged in autophagy-related signalling (Fig. 1b), especially macroautophagy (Fig. 1b(i)), showed the highest absolute value of enrichment scores (z -scores) in the Lhb among the many brain regions analysed in CRS mice. In addition, autophagy-related genes in the Lhb indicate downregulation of autophagy compared to the naive controls. Furthermore, single-nucleus RNA-seq (snRNA-seq) in the Lhb showed that autophagy-related genes show selective downregulation of autophagy in neurons rather than glial cells (Extended Data Fig. 3a). By contrast, enrichment of macroautophagy genes in the vHippo, VTA and NAc was undetectable, and significant enrichment of autophagy upregulation-related genes was detected in the lateral

hypothalamus but not significant in the mPFC (Fig. 1b(i)). Moreover, at the single gene level, we observed significantly decreased mRNA expression levels of genes involved in the autophagy activation processes (Extended Data Fig. 3b,c1,2) (for example, *Becn1* (encoding Beclin-1) and autophagy-related gene *Atg10*), as well as tendencies towards decreased *Atg4d*, *Atg12*, *Atg7*, *Atg5* and *LC3* (also known as *Map1lc3a*) (Extended Data Fig. 3c). We also found a tendency towards increased mRNA expression level of *Mtor*, whose activation inhibits autophagy processes (Extended Data Fig. 3c). These transcriptomic results were further validated using quantitative PCR (qPCR) (Extended Data Fig. 3d). Notably, negative correlations were found between the mRNA levels of core autophagy genes in the Lhb of each mouse and the corresponding individual immobility durations in the FST (Fig. 1c,d), indicating a direct link between impaired Lhb autophagy function and depression-like status. In addition, mRNA levels of ubiquitin–proteasome system, another main intracellular protein degradation system⁴, were unaffected in the Lhb by CRS (Extended Data Fig. 3e–g), indicating the functional specificity of altered Lhb autophagy in depression.

Bidirectional effects of stress

To decipher how stress affects and eventually dampens Lhb autophagy, we measured Lhb autophagy function in mice treated with many stressors (restraint, social defeat or footshock), which engage distinct sensory modalities (physical, psychosocial or noxious), either acutely or chronically (Fig. 1e). These chronic stress protocols are all well-accepted animal models of depression^{29,30,36}. Consistent with the transcriptome data, protein levels in the Lhb also indicate impaired autophagy in various chronically stressed mouse models. By contrast, acute stressors all significantly enhanced Lhb autophagy compared with naive mice (Fig. 1f,g). To investigate whether stress-induced neuronal activity directly enhances Lhb autophagy, we applied 40-Hz phasic photostimulation (4 pulses per second) at lateral hypothalamus-Lhb synaptic terminals, which mimics the neuronal firing pattern evoked by various acute stressors^{29,31}, and found that it also enhanced Lhb autophagy (Extended Data Fig. 4a,b), suggesting an activity-dependent enhancement of Lhb autophagy during acute stress.

We further measured autophagic flux either by immunostaining LC3 puncta in wild-type (WT) mice or quantifying puncta fluorescence in LC3-GFP reporter mice. Consistently, LC3 puncta fluorescence was enhanced in the Lhb of mice treated with acute restraint stress (ARS), whereas it was decreased in those treated with CRS (Fig. 1h,i and Extended Data Fig. 4c). Moreover, the number of autophagosomes detected under electron microscopy in Lhb neurons was drastically increased by ARS but decreased by CRS (Extended Data Fig. 4d). Consistent with the mRNA expression levels, the protein level of ubiquitin was also unaffected by acute or chronic stress (Fig. 1j–l). Notably, neither ARS nor CRS altered autophagy function in the vHippo (Extended Data Fig. 4e). In addition, food restriction, a classical trigger of autophagy in peripheral organs³⁷, enhanced autophagy in the liver without affecting the Lhb (Extended Data Fig. 4f,g).

Independent roles of AMPK and mTOR

Given that mTOR inhibition and AMP-activated protein kinase (AMPK) activation are two canonical inducers of autophagy², we determined the expression levels of phosphorylated AMPK (p-AMPK) and phosphorylated mTOR (p-mTOR) in the LHB of mice under either ARS or CRS. Western blot showed that ARS increased p-AMPK level without affecting p-mTOR or the downstream phosphorylated p70S6 kinase (p-S6K), whereas CRS augmented p-mTOR and p-S6K levels without affecting p-AMPK (Fig. 1m–p). Collectively, these results indicate the independent and opposing roles of AMPK and mTOR signalling in modulating LHB autophagy at different stages of stress. Acute stress activates AMPK to initiate LHB autophagy, whereas chronic stress activates mTOR to terminate LHB autophagy.

To determine whether AMPK is required for autophagy initiation during acute stress, SBI-0206965 (SBI), a selective inhibitor of AMPK-ULK1 (Unc51-like autophagy activating kinase 1) phosphorylation, was locally infused into the LHB before ARS, and subsequent western blot experiments of relevant signalling pathways were performed (Fig. 1q). We found that p62 level was increased, whereas Beclin-1 and p-AMPK levels were decreased by SBI, without altering p-mTOR and p-S6K levels (Fig. 1r–v), suggesting an indispensable role of AMPK activation in ARS-induced autophagy in the LHB. Excitatory synaptic transmission elevated by acute stress returned to basal levels 1–3 days after stress exposure (Extended Data Fig. 5a–d), indicating a naturally occurring process of synaptic depression. However, this reversal of synaptic potentiation was abolished under local blockade of LHB autophagy by means of SBI during the exposure to ARS (Extended Data Fig. 5a–d). Given the essential role of LHB synaptic potentiation in a depression-like state^{27–29,31}, our data indicate that a failure of naturally occurring synaptic depression may facilitate depression-like behaviours after acute stress. Indeed, local infusion of SBI facilitated an anhedonia-like phenotype in the sucrose preference test (SPT), without affecting the despair-like phenotype in the tail suspension test, as well as the locomotion and anxiety-like phenotype in the open field test (OFT) (Extended Data Fig. 5e–h). Altogether, these results indicate that AMPK signalling is required for the initiation of LHB autophagy to cope with acute stress.

Antidepressant role of LHB autophagy

Given that mTOR signalling is elevated after chronic stress, we tested whether mTOR inhibition alleviates depression-like behaviours. Therefore, rapamycin, a US Food and Drug Administration (FDA)-approved mTOR inhibitor was systemically injected in CRS mice (Fig. 2a). We found that rapamycin alleviated depression-like behaviours (Fig. 2b,c), without affecting OFT performance (Extended Data Fig. 6a). Notably, systemic treatment of rapamycin under antidepressant dosage enhanced autophagy in the LHB rather than other regions (Fig. 2d). To assess whether LHB autophagy is required for antidepressant-like actions of rapamycin, we designed a short hairpin RNA (shRNA) to knock down *Atg7* mRNA by means of viral gene transfer (Fig. 2e,f). Overexpression of *Atg7*-targeting shRNA (sh*Atg7*) specifically in the LHB abolished antidepressant-like effects of rapamycin in both FST and SPT (Fig. 2g,h), without altering OFT performance (Extended Data Fig. 6b). These results reveal the necessary role of LHB autophagy in the antidepressant effect of rapamycin.

To further interrogate whether activation of LHB autophagy is required for different antidepressants, we measured antidepressant-like effects of paroxetine and ketamine in mice with deficient LHB autophagy. Antidepressant-like effects of chronic paroxetine treatment were partially abolished by conditional knockout of *Atg7* specifically in the LHB (*Atg7^{LHB}-/-*), characterized by behavioural phenotypes in the FST and social interaction test (SIT), without affecting SPT performance (Fig. 2i–l). Similarly, ketamine showed no antidepressant-like effects in

Atg7^{LHB}-/- mice compared to vehicle-treated controls (Extended Data Fig. 7a–d). These findings indicate LHB autophagy as a common mechanistic target of antidepressant-like actions. Concerning the molecular pathways by which different antidepressants regulates LHB autophagy, both ketamine and paroxetine at antidepressant dosage decreased the levels of phosphorylated Akt (p-Akt) and p-mTOR in the LHB of CRS mice (Extended Data Fig. 7e–h). As reduced phosphorylation of Akt inhibits mTOR and thus activates Beclin-1 to promote autophagy²⁴, our findings suggest that various antidepressants might activate LHB autophagy through inhibiting Akt signalling.

As rapamycin, paroxetine and ketamine are all involved in other biological processes besides autophagy, we further assessed whether specific activation of LHB autophagy directly modulates depression-like behaviours. A selective agonist of Beclin-1, TAT–Beclin-1 peptide (tBP), was locally infused into bilateral LHB of mice after experiencing either CRS or chronic social defeat stress (CSDS) (Fig. 3a,f). tBP treatment enhanced LHB autophagy in the LHB (Fig. 3b), without affecting apoptosis (Extended Data Fig. 8a). tBP rapidly (within 0.5 h) reversed CRS- or CSDS-induced depression-like behaviours (Fig. 3c–e,g–i), without affecting OFT behaviour (Extended Data Fig. 6c,d). These results demonstrate that specific activation of LHB autophagy exerts rapid antidepressant-like effects in distinct animal models of chronic stress-induced depression.

To further investigate whether enhancing LHB autophagy exerts sustained antidepressant-like effects, we conducted behavioural tests at many time points following tBP infusion into the LHB of CRS mice (Extended Data Fig. 9a). Antidepressant-like actions of tBP on CRS mice maintained at least for 7 days postinfusion, however, disappeared 18–19 days postinfusion (Extended Data Fig. 9b–g). Moreover, to evaluate the prophylactic effects of enhancing LHB autophagy, we administered local tBP infusions during 14-day CRS and subsequently measured depression-like behaviours (Extended Data Fig. 9h). Such tBP treatment effectively prevented the development of depression-like behaviours (Extended Data Fig. 9i–k), without affecting OFT performance (Extended Data Fig. 9m). Notably, immobile duration in the tail suspension test 26 days posttreatment of tBP remains lower than the vehicle controls, thus confirming prophylactic effects, rather than sustained antidepressant-like effects, of tBP (Extended Data Fig. 9l).

Given that LHB hyperactivity is a cellular hallmark of depression-like status^{27–30,35,38}, we examined whether enhancing LHB autophagy directly normalized its neuronal hyperactivity (Fig. 3j). LHB neurons are spontaneously active and classified into three subtypes (silent, tonic and burst neurons) (Fig. 3k), among which burst firing is drastically enhanced in animal models of depression^{27,35,38}. After incubation with tBP in LHB slices of CRS mice, burst (Fig. 3l,m) and the overall spontaneous (Fig. 3n) firing activity were both largely attenuated in a dose-dependent manner. tBP incubation also weakened excitatory but not inhibitory neurotransmission (Fig. 3o–q), and decreased neuronal excitability (Extended Data Fig. 10a–c) of LHB neurons in CRS mice.

On-demand activation of brain autophagy

We found that the silencing effects of tBP were activity-dependent and thus less effective for less active LHB neurons in naive mice (Extended Data Fig. 10d–j). To further validate the activity-dependent activation of autophagy, we further interrogated several other brain regions that show hyperactivity under chronic stress, including the basolateral amygdala (BLA)³⁹ and the arcuate nucleus (Arc)⁴⁰. Western blot results revealed that CRS impairs autophagy function in the Arc but not the BLA (Extended Data Fig. 10k,l).

We then tested whether tBP modulated neuronal activity of pyramidal neurons in BLA slices or pro-opiomelanocortin (POMC) neurons in Arc slices from mice treated with CRS. We crossed POMC-Cre mice with *Ail14* mice to visualize POMC neurons, and found that tBP perfusion

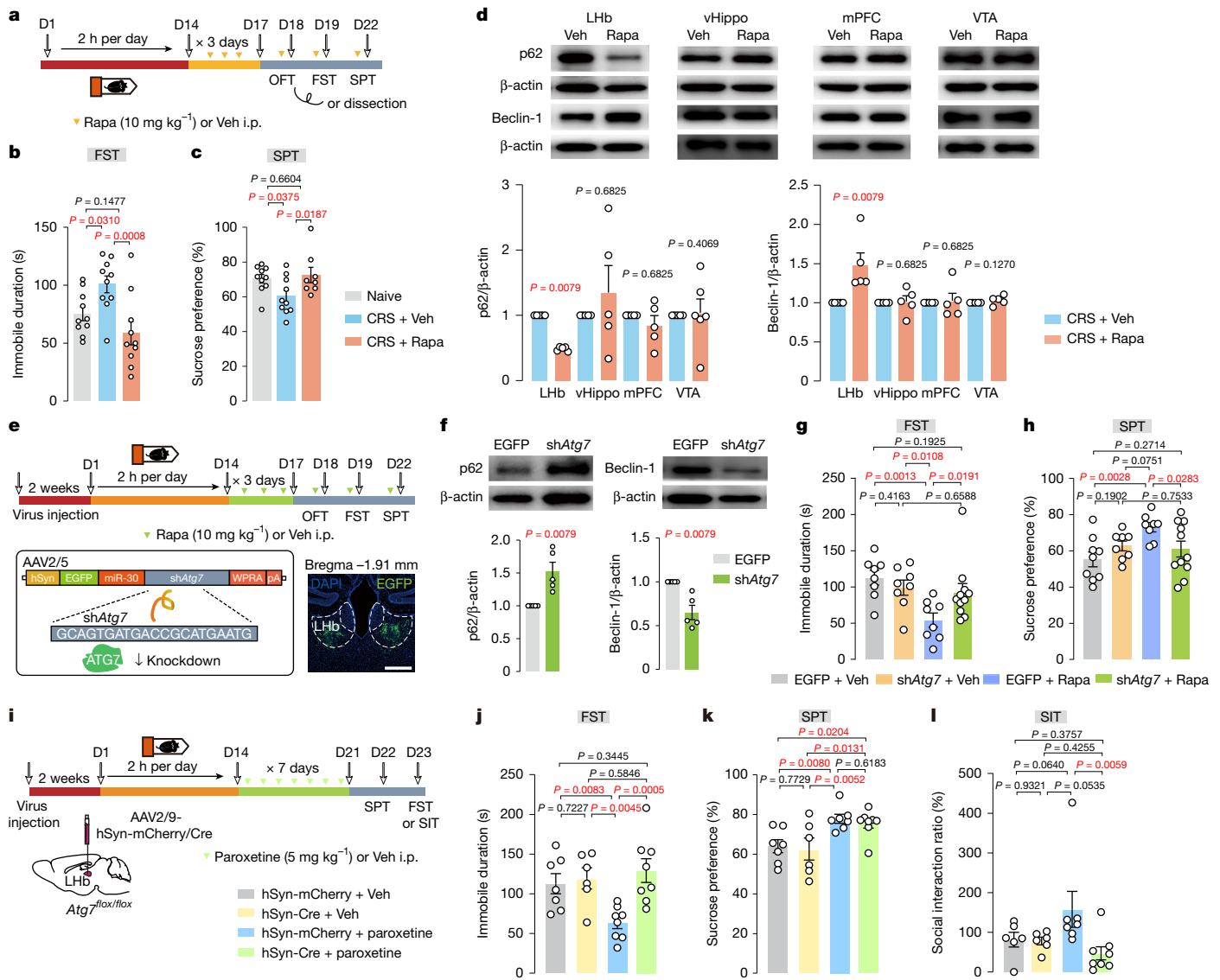


Fig. 2 | Actions of different antidepressants commonly require Lhb autophagy. **a**, Experimental design. Rapa, rapamycin; i.p., intraperitoneal injection. **b, c**, Intraperitoneal injection of rapamycin alleviates depression-like phenotypes (**b**, $n_{\text{naive/CRS+Veh/CRS+Rapa}} = 10$ per group; **c**, $n_{\text{naive/CRS+Veh/CRS+Rapa}} = 10, 10, 8$). **d**, Intraperitoneal injection of rapamycin enhances autophagy selectively in Lhb but not vHippo, mPFC and VTA of CRS mice (p62, $n_{\text{CRS+Veh/CRS+Rapa}} = 5, 6$ for VTA, $n_{\text{CRS+Veh/CRS+Rapa}} = 5$ per group for the rest of brain regions; Beclin-1, $n_{\text{CRS+Veh/CRS+Rapa}} = 5$ per group). **e**, Experimental design, shRNA working model and a representative image of viral expression. Scale bar, 500 μm . **f**, Representative images (top) and quantification (bottom) of p62 and Beclin-1 western blot from Lhb lysates, showing that *Atg7* knockdown decreases Lhb autophagy

(that is, increased p62 and decreased Beclin-1) ($n_{\text{EGFP/shAtg7}} = 5$ per group for p62 and Beclin-1). **g, h**, Knockdown of *Atg7* in Lhb abolishes antidepressant-like effects of rapamycin in CRS mice (**g**, $n_{\text{EGFP+Veh/shAtg7+Veh/EGFP+Rapa/shAtg7+Rapa}} = 8, 8, 11, 8$; **h**, $n_{\text{EGFP+Veh/shAtg7+Veh/EGFP+Rapa/shAtg7+Rapa}} = 9, 8, 11, 8$). **i**, Experimental design. **j–l**, Conditional knockout of *Atg7* in Lhb abolishes antidepressant-like effects of paroxetine in FST (**j**, $n_{\text{mCherry+Veh/cre+Veh/mCherry+Pxt/cre+Pxt}} = 7, 6, 8, 8$) and SIT (**l**, $n_{\text{mCherry+Veh/cre+Veh/mCherry+Pxt/cre+Pxt}} = 6/6/7/8$), but not SPT (**k**, $n_{\text{mCherry+Veh/cre+Veh/mCherry+Pxt/cre+Pxt}} = 7, 6, 7, 8$). Two-sided Mann–Whitney test (**d, f**) and one-way ANOVA with uncorrected Fisher’s least significant difference (LSD) test (**b, c, g, h, j–l**). Data are mean \pm s.e.m. Schematics in **a, e, i** adapted from ref. 31, Elsevier.

rapidly decreased both neuronal excitability and excitatory neurotransmission in POMC neurons but not BLA pyramidal neurons (Extended Data Fig. 10m–t). As neuronal excitability and excitatory synaptic transmissions of Arc POMC neurons are much higher than BLA pyramidal neurons, whereas they are comparable to Lhb neurons (Extended Data Fig. 10u, v), these findings suggest that autophagy is activated in more active neurons.

We speculated that Lhb autophagy is activated in an ‘on-demand’ manner to degrade excessive membrane proteins. Indeed, we observed increased protein levels of GluA1, GluA2 and GluN1 subunits of glutamate receptors (GluRs), but not the GABA_A subunit of GABA (γ -aminobutyric acid) receptors in membrane fractions of Lhb from CRS mice (Fig. 4a–d). Conversely, local infusion of tBP in the Lhb rapidly

reversed the membrane protein levels of GluRs (Fig. 4e–h), indicating that enhancing Lhb autophagy is sufficient to promote degradation of excessive GluRs in an on-demand manner.

Moreover, the mRNA levels of T-type calcium channel (T-VSCC) and inwardly rectifying potassium channel Kir2.1, two potential candidates engaged in controlling Lhb neuronal excitability^{35,41}, were unaltered by CRS (Extended Data Fig. 3h, i). In line with the unaltered current intensity of T-VSCC in CRS mice³⁵, these findings indicate unaltered T-VSCC function in CRS mice. In addition, consistent with the relatively depolarized resting membrane potential (roughly -50 mV) of Lhb neurons^{35,38}, the amount of *Kir2.1* mRNA in the Lhb was scarce (Extended Data Fig. 3h), suggesting the low contribution of Kir2.1 to Lhb neuronal excitability.

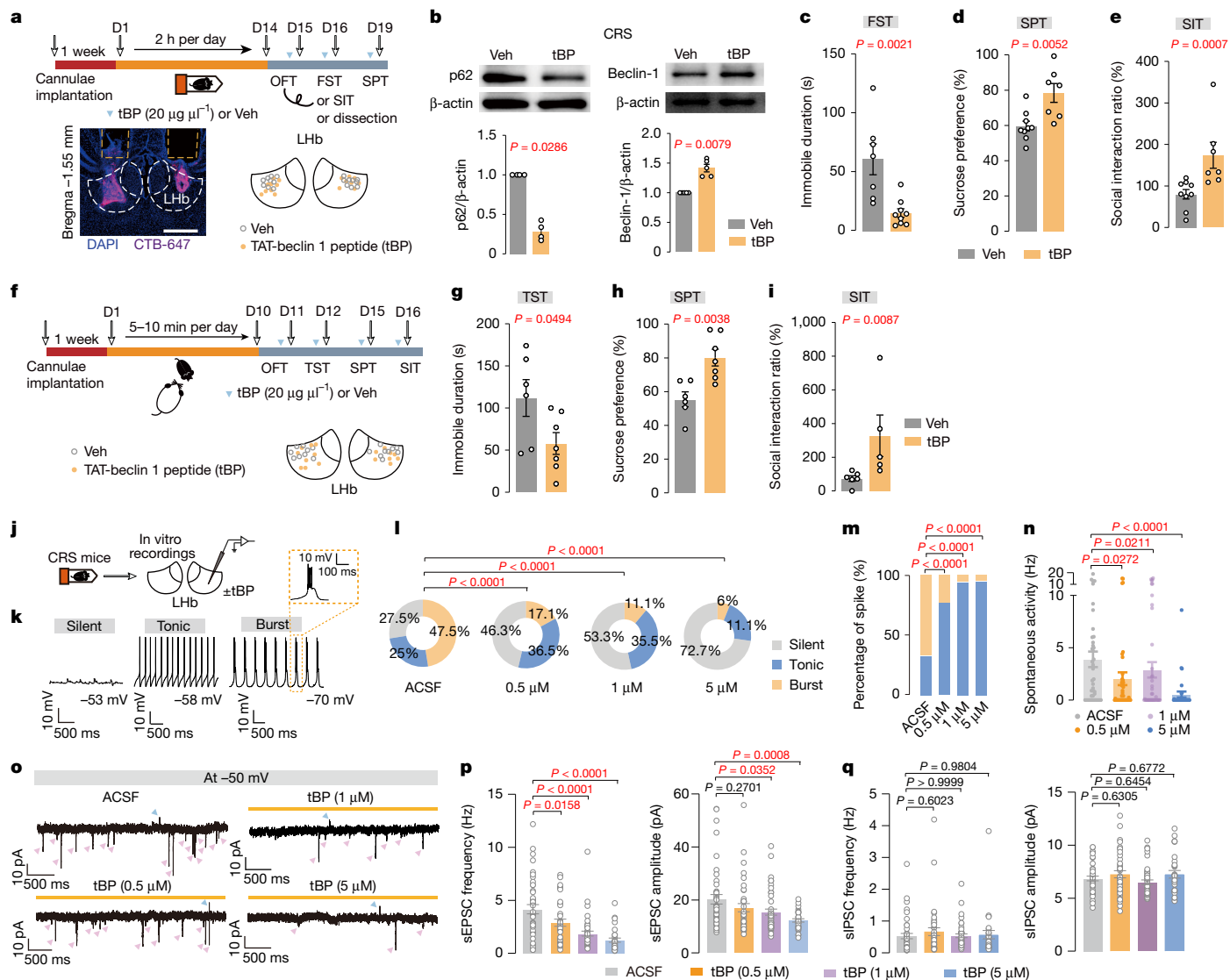


Fig. 3 | Enhancing LHB autophagy rapidly exerts antidepressant-like effects by means of normalization of neuronal hyperactivity and synaptic deficit in chronic stressed mice. **a**, Experimental designs, representative illustrations of bilateral implantation of cannulae and drug infusion sites. Scale bar, 500 μm . **b**, Representative images (top) and quantification (bottom) of western blot show that local infusion of tBP instantly increases LHB autophagy (that is, decreased p62 and increased Beclin-1) (tested within 30 min after tBP infusion; p62, $n_{\text{Veh/tBP}} = 4$ per group; Beclin-1, $n_{\text{Veh/tBP}} = 5$ per group). **c–e**, LHB local infusion of tBP rapidly alleviates depression-like phenotypes in CRS mice (**c**, $n_{\text{Veh/tBP}} = 7, 9$; **d**, $n_{\text{Veh/tBP}} = 9, 7$). **f**, Experimental design. **g–i**, Local infusion of tBP in LHB rapidly alleviates depression-like phenotypes in CSDS mice (**g**, $n_{\text{Veh/tBP}} = 6, 7$; **h**, $n_{\text{Veh/tBP}} = 6, 5$). **j**, Experimental design. **k**, Representative traces showing spontaneous activity ($I = 0$) of silent (left), tonic-firing (middle) and burst-firing (right) LHB neurons recorded with whole-cell patch clamp. **l–n**, Pie charts (**l**, $n_{\text{ACSF/0.5 } \mu\text{M}} = 40, 41, 45, 33$ neurons; $n_{\text{ACSF/0.5 } \mu\text{M}} = 8, 6, 7, 8$ mice),

histograms (**m**, $n_{\text{ACSF/0.5 } \mu\text{M}} = 40, 41, 45, 33$ neurons; $n_{\text{ACSF/0.5 } \mu\text{M}} = 8, 6, 7, 8$ mice) and bar graphs (**n**, $n_{\text{ACSF/0.5 } \mu\text{M}} = 40, 41, 43, 33$ neurons; $n_{\text{ACSF/0.5 } \mu\text{M}} = 8, 6, 7, 8$ mice) showing dose-dependent effects of tBP on spontaneous firing patterns, percentage of spikes and firing frequencies of LHB neurons in CRS mice. ACSF, artificial cerebrospinal fluid. **o–q**, Representative traces (**o**) and quantification (frequency (**p**) and amplitude (**q**)) showing dose-dependent effects of tBP on synaptic transmission onto LHB neurons in CRS mice (**p**, $n_{\text{ACSF/0.5 } \mu\text{M}} = 43, 39, 44, 30$ neurons; $n_{\text{ACSF/0.5 } \mu\text{M}} = 8, 6, 7, 8$ mice; **q**, $n_{\text{ACSF/0.5 } \mu\text{M}} = 42, 39, 44, 29$ neurons; $n_{\text{ACSF/0.5 } \mu\text{M}} = 8, 6, 7, 8$ mice). Blue or pink arrowheads indicate spontaneous excitatory and inhibitory postsynaptic current (sEPSC and sIPSC, respectively) events. Two-sided unpaired *t*-test (**g, h**), two-sided Mann–Whitney test (**b–e, i**), one-way ANOVA with Dunn’s multiple comparisons test (**p, q**), Kruskal–Wallis test with uncorrected Dunn’s test (**n**) and two-sided chi-square test (**l, m**). Data are mean \pm s.e.m. Schematics in **a, f, j** adapted from ref. 31, Elsevier.

To further validate whether LHB autophagy specifically targets synaptic GluRs, we first determined the subcellular localization of LHB autophagic markers in ARS mice. We performed immunostaining to measure the colocalization of LC3 puncta and PSD95, and found that roughly 80% of LC3 puncta was colocalized with PSD95 in the LHB of ARS mice, indicating predominant postsynaptic localization of autophagic flux in the LHB (Extended Data Fig. 11a,b). We also directly visualized colocalization of GluA2 and LC3 puncta in the LHB of ARS mice with stochastic optical reconstruction microscopy (STORM) (Extended Data

Fig. 11c and Supplementary Video 1). The colocalization of GluA2 was also observed in more active Arc neurons, but rarely in less active BLA neurons (Extended Data Fig. 11c and Supplementary Videos 2 and 3), suggesting that autophagy selectively targets GluRs in more active brain regions. Furthermore, immunoelectron microscopy showed that the number of GluA2-containing autophagosomes were increased by ARS, whereas decreased by CRS (Extended Data Fig. 11d,e). Collectively, these results indicate that LHB autophagy primarily degrades postsynaptic GluRs.

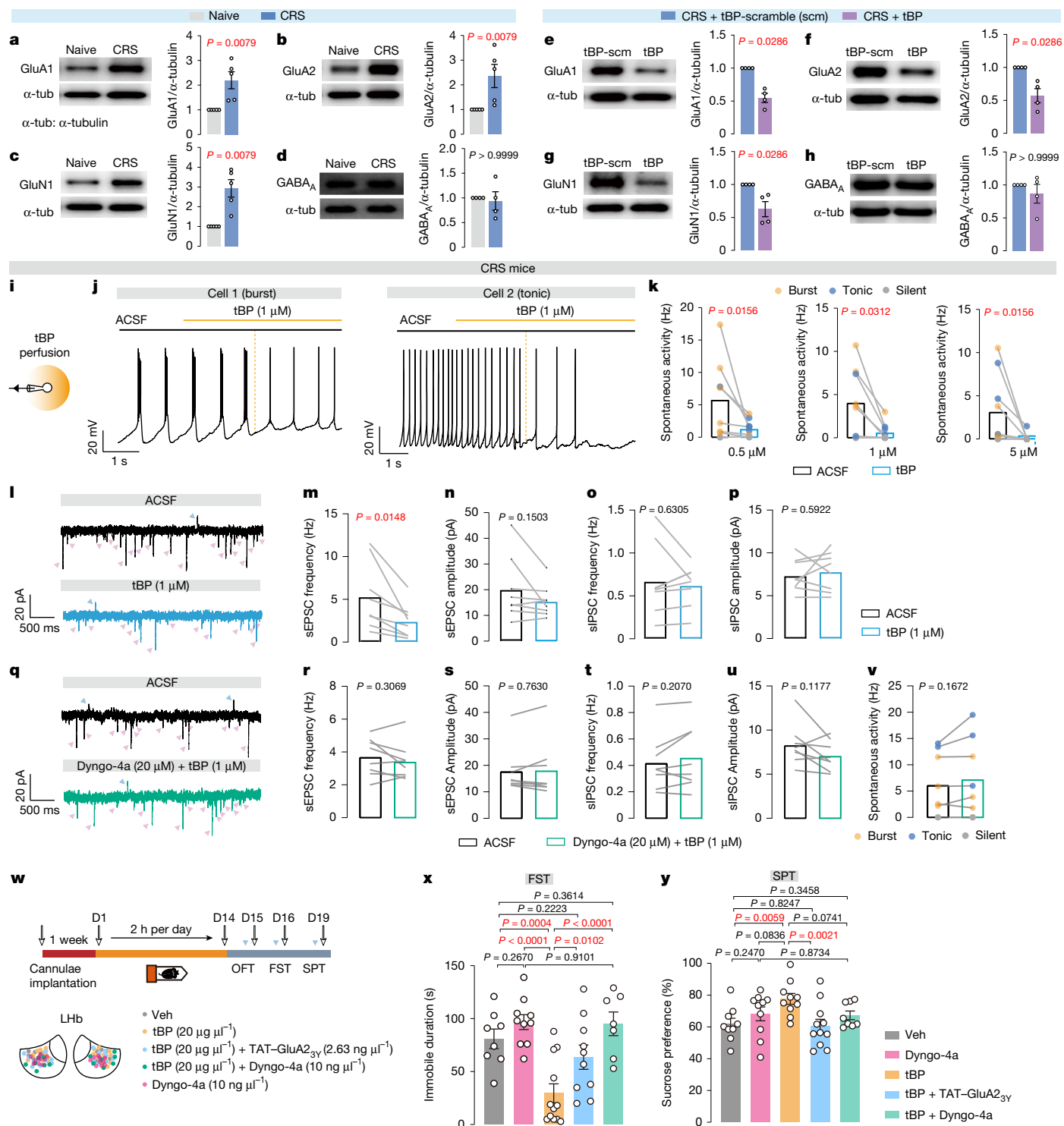


Fig. 4 | Enhancing LHB autophagy facilitates synaptic GluRs degradation for normalizing neuronal hyperactivity and depression-like behaviours. **a–h**, Western blot analysis showing that CRS (**a–d**) increased, whereas activating LHB autophagy by local infusion of tBP (**e–h**) decreased, the expression of GluA1 (**a,e**), GluA2 (**b,f**) and GluN1 (**c,g**), without affecting the GABA_A receptor subunit (**d,h**) (**a–c**, $n_{\text{naive/CRS}} = 5$ per group; **d**, $n_{\text{naive/CRS}} = 4$; **e–h**, $n_{\text{CRS+tBP-scramble/CRS+tBP}} = 4$ per group). α -tub, α -tubulin **i**, Experimental design. **j,k**, Representative traces (**j**) and quantification (**k**) show the acute effect of tBP perfusion on spontaneous firing patterns and firing frequency of LHB neurons ($n_{\text{ACSF/0.5/1/5}} = 8, 8, 9$ neurons, $n_{\text{ACSF/0.5/1/5}} = 7, 6, 6$ mice). **l–p**, Representative traces (**l**) and quantification (frequency (**m,o**) and amplitude (**n,p**) of sEPSC and sIPSC) showing spontaneous neural transmission before and right after tBP perfusion in LHB neurons of CRS mice (1 μ M tBP, $n_{\text{ACSF/tBP}} = 8$ neurons, $n_{\text{ACSF/tBP}} = 6$ mice). **q–u**, Representative

traces (**q**) and quantification (**r–u**) showing spontaneous neural transmission before and right after coprefusion of tBP and Dyngo-4a in LHB neurons of CRS mice (Dyngo-4a + 1 μ M tBP, $n_{\text{ACSF/Dyngo+tBP}} = 8$ neurons, $n_{\text{ACSF/Dyngo+tBP}} = 3$ mice); sEPSC frequency (**r**), sEPSC amplitude (**s**), sIPSC frequency (**t**) and sIPSC amplitude (**u**). **v**, Bar graph showing spontaneous firing frequency before and after coprefusion of tBP and Dyngo-4a (Dyngo-4a + 1 μ M tBP, $n_{\text{ACSF/Dyngo+tBP}} = 8$ neurons, $n_{\text{ACSF/Dyngo+tBP}} = 3$ mice). **w**, Experimental design. **x,y**, tBP decreases immobile duration in FST (**x**) and increases sucrose preference in SPT (**y**) whereas co-application of tBP with Dyngo-4a or TAT-GluA2_{3Y} reverses this effect (**x**, $n_{\text{Veh/Dyngo/tBP/tBP+TAT-GluA23y/Dyngo+tBP}} = 8, 10, 12, 10, 7$; **y**, $n_{\text{Veh/Dyngo/tBP/tBP+TAT-GluA23y/Dyngo+tBP}} = 9, 10, 10, 11, 8$). Two-sided Mann-Whitney test (**a–h**), two-sided paired *t*-test (**k,m–p,r–v**), two-sided Wilcoxon test (**a–h**), two-sided paired *t*-test (**k,m–p,r–v**), two-sided Wilcoxon test (**k**), one-way ANOVA with uncorrected Fisher's LSD test (**x,y**). Data are mean \pm s.e.m. Schematic in **w** adapted from ref. 31, Elsevier.

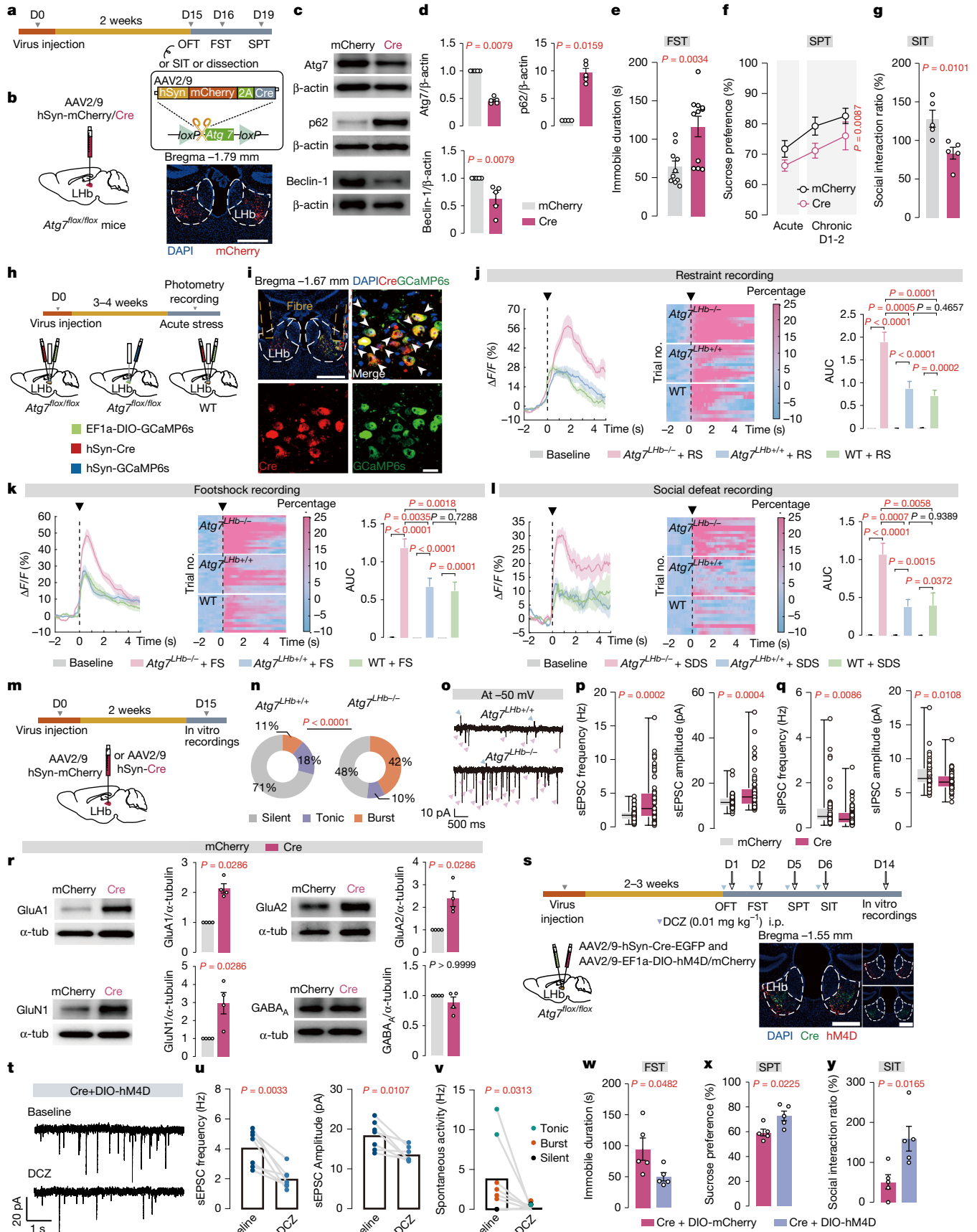


Fig. 5 | See next page for caption.

Fig. 5 | Genetic ablation of LHB neuronal autophagy directly elicits depression-like phenotypes and neuronal hyperactivity. **a**, Experimental design. **b**, Viral strategy. **c, d**, Representative images (**c**) and quantification (**d**) of Atg7, p62 and Beclin-1 western blot showing decreased autophagy in LHB of *Atg7^{LHb-/-}* mice (**d**, *Atg7^{LHb-/-}; n_{mCherry/Cre}* = 5 per group, p62: *n_{mCherry/Cre}* = 4/5, Beclin-1: *n_{mCherry/Cre}* = 5 per group). **e–g**, *Atg7^{LHb-/-}* mice showed depression-like phenotypes (**e** and **f**, *n_{mCherry/Cre}* = 10/11; **g**, *n_{mCherry/Cre}* = 5 per group). **h**, Experimental designs. **i**, Representative images of histology. White arrowheads: colocalization of GCaMP6s and Cre. Scale bars: 500 μ m (top), 20 μ m (bottom). **j–l**, Averaged responses (left), heat maps (middle) and area under the curve (AUC) (right) showing Ca²⁺ signals in LHB neurons evoked by stressors (**j**, *n_{Atg7^{-/-}→RS/Atg7^{+/+}RS/WT+RS}* = 12, 14, 10 trials; 3, 3, 3 mice; **k**, *n_{Atg7^{-/-}→FS/Atg7^{+/+}FS/WT+FS}* = 17, 15, 14 trials; 3, 4, 4 mice; **l**, *n_{Atg7^{-/-}→SDS/Atg7^{+/+}SDS/WT+SDS}* = 14, 13, 11 trials; 3, 3, 3 mice). **m**, Experimental design. **n**, Pie charts illustrating the percentage of three neuronal subtypes in LHB (*n_{Atg7^{+/+}/Atg7^{-/-}}* = 55, 64 neurons; 6, 6 mice). **o–q**, Representative traces (**o**) and

quantification (**p**, *n_{Atg7^{+/+}/Atg7^{-/-}}* = 53, 64 neurons; 6, 6 mice; **q**, *n_{Atg7^{+/+}/Atg7^{-/-}}* = 51/61 neurons, 6/6 mice) showing that *Atg7* deficiency alters LHB synaptic transmission. **r**, Western blot analysis of GluA1, GluA2, GluN1 and GABA_A expression in LHB of *Atg7^{LHb+/+}* and *Atg7^{LHb-/-}* mice (*n_{mCherry/Cre}* = 4 per group). **s**, Chemogenetic strategy and representative images of histology. **t–v**, Representative traces (**t**) and quantification showing the effect of deschloroclozapine (DCZ) on sEPSCs (*n* = 7 neurons, three mice) (**u**) and spontaneous activity (*n* = 8 neurons, three mice) (**v**). **w–y**, Chemogenetic silencing of LHB neurons rescues depression-like phenotypes in FST (**w**), SPT (**x**) and SIT (**y**) in *Atg7^{LHb-/-}* mice (*n_{DIO-mCherry/DIO-hM4D}* = 5 per group). Two-sided Mann–Whitney test (**d, p–r**), two-sided unpaired *t*-test (**e, g, w–y**), two-sided paired *t*-test (**u**), two-sided unpaired *t*-test and two-sided paired *t*-test (**j–l**), two-sided Wilcoxon test (**v**), two-way ANOVA (**f**) and two-sided chi-square test (**n**). Data are mean \pm s.e.m. Scale bar, 500 μ m (**b, s**). Schematics in **b, h, m, s** adapted from ref. 29, Elsevier.

To further measure the onset time of tBP actions in LHB neuronal and synaptic activity, tBP was directly perfused onto LHB slices of CRS mice (Fig. 4i). We found that tBP immediately (within seconds) abolished burst and tonic-firing activity (Fig. 4j,k), decreased neuronal excitability (Extended Data Fig. 12a–c), and attenuated excitatory rather than inhibitory neurotransmission of LHB neurons in a dose-dependent manner (Fig. 4l–p and Extended Data Fig. 12d,e). Such instant silencing effects suggest that tBP exerts rapid antidepressant-like effects by means of directly normalizing LHB neuronal and synaptic hyperactivity.

Coperfusion of tBP with Dyngo-4a, an endocytosis blocker, completely abolished such instant silencing effects (Fig. 4q–v), indicating a necessary role of endocytosis in LHB autophagy-mediated rapid degradation of GluRs. At the behavioural level, co-infusion of either Dyngo-4a or TAT–GluA2₃₃ (a specific blocker targeting the endocytosis of GluA2 subunit) completely abolished the antidepressant-like effects of tBP (Fig. 4w–y), without affecting OFT performance (Extended Data Fig. 6e). Altogether, these findings indicate GluRs as primary targets of autophagy-mediated degradation for reversing LHB hyperactivity and depression-like behaviours.

Loss-of-function of LHB autophagy

To interrogate the causal role of impaired LHB autophagy in depression-like state, we used a viral strategy to conditionally knock out *Atg7* specifically in LHB neurons of naive mice, and performed subsequent biochemical and behavioural identifications (Fig. 5a). Local knockout of *Atg7* in LHB of *Atg7^{lox/lox}* mice (*Atg7^{LHb-/-}*) (Fig. 5b) decreased LHB neuronal autophagy (Fig. 5c,d), without affecting apoptosis (Extended Data Fig. 8b,c). Moreover, *Atg7^{LHb-/-}* mice showed increased depression-like behaviours (Fig. 5e–g), without altering OFT performance (Extended Data Fig. 6f). These depression-like phenotypes were absent under hemi-knockout of LHB neuronal *Atg7* in *Atg7^{lox/+}* heterozygotes (Extended Data Fig. 13a). To cross-validate the consequences of virally genetic ablation of LHB neuronal autophagy, we further deployed shRNA viral strategy to knock down the mRNA of *Atg7*, *Atg5* or *Becn1* in LHB neurons of naive mice, and reproduced depression-like behaviours similar to stress-naive *Atg7^{LHb-/-}* mice (Extended Data Fig. 13bd). In addition, *Atg7* deficiency in either LHB astrocytes or vHippo neurons did not affect depression-like phenotypes (Extended Data Fig. 13e,f), indicating that depression-like state gated by autophagy occurs in specific brain regions and cell types.

To dissect the neuronal substrate of depression-like behaviours induced by disrupted LHB neuronal autophagy, we monitored calcium responses to stressors in autophagy-deficient LHB neurons of freely moving *Atg7^{LHb-/-}* mice, using a dual-viral strategy (Fig. 5h,i). *Atg7^{LHb-/-}* neurons showed twofold larger calcium responses to many stressors (restraint, footshock and social defeat) compared to the viral and strain controls (Fig. 5j–l), suggesting increased stress-encoding efficiency in *Atg7^{LHb-/-}* neurons in vivo. To deconstruct the effects of impaired

autophagy on LHB neurons, we measured firing activity and neurotransmissions in LHB neurons with either *Atg7* or *Atg5* ablation (Fig. 5m and Extended Data Fig. 13g–j). *Atg7*- or *Atg5*-deficient LHB neurons showed hyperactivity that was manifested as enhanced bursting activity (Fig. 5n and Extended Data Fig. 13g), increased excitatory neurotransmission and decreased inhibitory neurotransmission (Fig. 5o–q and Extended Data Fig. 13h–j). We also observed increased protein levels of GluA1, GluA2 and GluN1 subunits, but not GABA_A subunits in membrane fractions of LHB from *Atg7^{LHb-/-}* mice (Fig. 5r), suggesting a constitutive role of autophagy in degrading synaptic GluRs and thus maintaining neuronal homeostasis in the LHB. To investigate whether LHB hyperactivity induced by *Atg7* loss-of-function directly links autophagy impairment with depression-like state, we examined whether these depression-like phenotypes in *Atg7^{LHb-/-}* mice were reversed by normalizing LHB hyperactivity. Using a dual-viral strategy, we chemogenetically silenced autophagy-deficient LHB neurons (Fig. 5s–v), which successfully alleviated depression-like behaviours in *Atg7^{LHb-/-}* mice (Fig. 5w–y), without affecting OFT performance (Extended Data Fig. 6g). These results indicate that LHB hyperactivity serves as a cellular basis of depression-like state induced by impaired LHB autophagy.

Autophagy controls LHB plasticity

The balance between synthesis and degradation of synaptic proteins is fundamental for the magnitude and occurrence rate of synaptic plasticity, which affects LHB hyperactivity and depression-like state^{27–29,31}. Given that autophagy has been considered necessary for long-term depression (LTD)^{11,12,14,16}, we determined whether LTD was affected in LHB neurons of CRS mice. Through optogenetic targeting of lateral hypothalamus–LHB synapses, of which the potentiation mediates the onset of depression-like state during chronic stress^{29,31}, we discovered that low-frequency stimulation (LFS) rapidly upregulated autophagy (Extended Data Fig. 14a,b) and induced LTD (Extended Data Fig. 14d) in the LHB of naive mice. By contrast, LFS at lateral hypothalamus–LHB synapses failed to elevate autophagy (Extended Data Fig. 14a,c) and induce LTD (Extended Data Fig. 14d) in the LHB of CRS mice. Collectively, these results indicate a direct link between activating LHB autophagy and LTD induction. Indeed, autophagy inhibitor SBI abolished LFS-induced LTD and even promoted a slight but significant synaptic potentiation in LHB neurons of naive mice, without affecting basal neurotransmission (Extended Data Fig. 14e). We next determined whether LTD was also affected in *Atg7^{LHb-/-}* neurons (Extended Data Fig. 14f). LFS-induced LTD at lateral hypothalamus–LHB synapses was completely abolished in *Atg7^{LHb-/-}* neurons compared to *Atg7^{LHb+/+}* control groups (Extended Data Fig. 14g). The long-term potentiation (LTP) induction protocol^{29,31} evoked a higher magnitude of synaptic potentiation in *Atg7^{LHb-/-}* neurons compared to *Atg7^{LHb+/+}* control groups (Extended Data Fig. 14h), indicating that blockade of LHB autophagy causes further accumulation of postsynaptic GluRs under LTP induction.

To evaluate whether enhancing LHB autophagy was sufficient to reverse the LTD deficits, we perfused tBP onto LHB slices of CRS mice and discovered that tBP directly induced pharmacological LTD in a dose-dependent manner (Extended Data Fig. 14i). This pharmacological LTD was completely blocked by TAT–GluA2_{3Y} peptide (Extended Data Fig. 14j), revealing a necessary role of GluR endocytosis in LTD induced by LHB autophagy. Moreover, this pharmacological LTD was entirely abolished in *Atg7^{Lhb-/-}* neurons (Extended Data Fig. 14k), suggesting that canonical autophagy signalling (Extended Data Fig. 3b) is responsible for the actions of tBP in modulating synaptic transmission in the LHB. Collectively, these results indicate that LHB neuronal autophagy controls the occurrence rate and magnitude of synaptic plasticity.

Discussion

The core theory of stress proposed by Hans Selye⁴² proposes that the brain experiences three stages during the accumulation of stress: alarm reaction, resistance and exhaustion (Extended Data Fig. 15). In accordance with Selye's theory, we propose that LHB autophagy is rapidly switched on by means of AMPK phosphorylation, acting as the 'alarm reaction' phase of stress. As stress exposure persists, excitatory afferents onto the LHB are gradually potentiated²⁹, and LHB autophagy may be constantly recruited for degrading excessive synaptic GluRs, resulting in the 'resistance' phase. During the late phase of chronic stress, LHB autophagy is suppressed by the over-activation of mTOR signalling. Consequently, LHB autophagy is incapable of counterbalancing the excessive synaptic weight through GluR degradation, causing the 'exhaustion' phase of stress, neuronal hyperactivity and depression-like phenotypes. Our study provides proof-of-concept evidence that LHB autophagy in vivo serves as a cellular substrate underlying the three stages of stress dynamics and gating depression-like state. We have clarified a causal role of LHB autophagy-dependent GluR degradation in confining the neuronal hyperactivity and excessive synaptic strength when coping with stress.

Our work also provides an in vivo conceptual framework for elucidating the roles of autophagy in different brain functions. As autophagy genes are extensively expressed in the nervous system, it is of particular interest why autophagosomes are rarely present in intact brains under basal conditions³⁷. Indeed, many brain autophagy studies were completed in invertebrates or cultured systems, so in vivo evidence is insufficient concerning how brain autophagy is activated in live mammalian brains. Our findings provide direct evidence that LHB autophagy is activated under stress conditions in vivo. Combined with functional characterizations by using slice recordings and behavioural assays, our results extend the conclusion from the recent discovery in cultured neurons that autophagy degrades synaptic GluRs⁴³.

Understanding how autophagy is differentially engaged in discrete cell types and specialized neural circuits will pave the way to develop new treatments for autophagy-related diseases. Our findings also indicate that only a small number of brain regions fit the profile of a primary target for autophagy enhancers: namely that they are naturally active, become overactive in depression and experience disruption of autophagy functions following chronic stress. Autophagy may act in an on-demand mode that active neurons require more activation of autophagy and therefore facilitate the exhaustion of autophagy functions. It would be intriguing to investigate whether this hypothesis extends as a general principle in the brain, potentially enabling autophagy enhancers to specifically target brain regions with higher metabolic demands.

AMPK and mTOR in the LHB are potential biomarkers at different stages of stress-induced depression (for example, subclinical and clinical depression), therefore serving as potential targets of preventative interventions (resilience incubation) and treatments, respectively. As a clinically approved mTOR-specific inhibitor, rapamycin has potential antidepressant effects both in patients with major depressive

disorder and animal models of depression^{44,45}. Our study provides further evidence that brain region-specific autophagy activation in the LHB is required for rapamycin to mitigate depression-like behaviours. It also provides a mechanistic explanation of why rapamycin largely strengthens the antidepressant efficacy of ketamine in patients with depression⁴⁴.

LHB-specific autophagy activation was also required for antidepressant actions of both paroxetine and ketamine, suggesting LHB autophagy as a common mechanistic target of different antidepressants. Given that SSRIs rapidly increase serotonin levels but their antidepressant actions require weeks to months, the delayed activation of LHB autophagy may underlie the therapeutic delay of SSRIs. Moreover, the persistent upregulation of LHB autophagy at least 24 h after systemic treatment of ketamine may underlie the sustained antidepressant effects of ketamine. Antidepressant actions of various drugs engage Akt signalling⁴⁶, of which reduced phosphorylation inhibits mTOR and activates autophagic processes²⁴. As both ketamine and paroxetine inhibit Akt–mTOR signalling in the LHB, our study discovers a molecular link between autophagy and a well-known antidepressant signalling.

Notably, the effects of different antidepressants on Akt–mTOR signalling depend on the brain regions in question. Previous studies revealed that activation of brain-derived neurotrophic factor (BDNF)–Akt–mTOR signalling in the hippocampus is crucial for the antidepressant actions of various medications^{47,48}. However, activation of BDNF signalling in the LHB causally mediates depression-like behaviours⁴⁹. As BDNF activation strongly activates Akt–mTOR signalling and thus inhibits autophagy, these findings are accordant with the possibility that antidepressant actions occur by inhibiting Akt–mTOR and activating autophagy in the LHB.

LHB-specific ablation of neuronal autophagy fully recapitulated the molecular, cellular and behavioural profiles induced by chronic stress, strongly indicating the physiological relevance of impaired LHB autophagy in the pathogenesis of depression-like state. Considering the instant reversal of LHB hyperactivity and rapid antidepressant-like actions by means of enhancing LHB autophagy, our study proposes a fascinating possibility that LHB autophagy serves as a new cellular target of rapid antidepressants. Enhancing LHB autophagy also exerts sustained antidepressant-like and prophylactic effects, highlighting the advantage of targeting autophagy as a promising interventional strategy. Collectively, autophagy enhancers may shed light on a new strategy for rapid antidepressant discovery.

Online content

Any methods, additional references, Nature Portfolio reporting summaries, source data, extended data, supplementary information, acknowledgements, peer review information; details of author contributions and competing interests; and statements of data and code availability are available at <https://doi.org/10.1038/s41586-025-08807-4>.

1. McEwen, B. S. et al. Mechanisms of stress in the brain. *Nat. Neurosci.* **18**, 1353–1363 (2015).
2. Griffey, C. J. & Yamamoto, A. Macroautophagy in CNS health and disease. *Nat. Rev. Neurosci.* **23**, 411–427 (2022).
3. Herrman, H. et al. Time for united action on depression: a Lancet–World Psychiatric Association Commission. *Lancet* **399**, 957–1022 (2022).
4. Soykan, T., Haucke, V. & Kuijpers, M. Mechanism of synaptic protein turnover and its regulation by neuronal activity. *Curr. Opin. Neurobiol.* **69**, 76–83 (2021).
5. Levine, B. & Kroemer, G. Biological functions of autophagy genes: a disease perspective. *Cell* **176**, 11–42 (2019).
6. Deng, Z. et al. Autophagy receptors and neurodegenerative diseases. *Trends Cell Biol.* **27**, 491–504 (2017).
7. Fleming, A. et al. The different autophagy degradation pathways and neurodegeneration. *Neuron* **110**, 935–966 (2022).
8. Hernandez, D. et al. Regulation of presynaptic neurotransmission by macroautophagy. *Neuron* **74**, 277–284 (2012).
9. Hill, S. E. & Colón-Ramos, D. A. The journey of the synaptic autophagosome: a cell biological perspective. *Neuron* **105**, 961–973 (2020).

10. Kuijpers, M. et al. Neuronal autophagy regulates presynaptic neurotransmission by controlling the axonal endoplasmic reticulum. *Neuron* **109**, 299–313.e9 (2021).
11. Pan, Y. et al. Neuronal activity recruits the CRT1/CREB axis to drive transcription-dependent autophagy for maintaining late-phase LTD. *Cell Rep.* **36**, 109398 (2021).
12. Shehata, M., Matsumura, H., Okubo-Suzuki, R., Ohkawa, N. & Inokuchi, K. Neuronal stimulation induces autophagy in hippocampal neurons that is involved in AMPA receptor degradation after chemical long-term depression. *J. Neurosci.* **32**, 10413–10422 (2012).
13. Yang, S. et al. Presynaptic autophagy is coupled to the synaptic vesicle cycle via ATG-9. *Neuron* **110**, 824–840.e10 (2022).
14. Compans, B. et al. NMDAR-dependent long-term depression is associated with increased short term plasticity through autophagy mediated loss of PSD-95. *Nat. Commun.* **12**, 2849 (2021).
15. Bourdenx, M. et al. Chaperone-mediated autophagy prevents collapse of the neuronal metastable proteome. *Cell* **184**, 2696–2714.e25 (2021).
16. Kallergi, E. et al. Dendritic autophagy degrades postsynaptic proteins and is required for long-term synaptic depression in mice. *Nat. Commun.* **13**, 680 (2022).
17. Shehata, M. et al. Autophagy enhances memory erasure through synaptic destabilization. *J. Neurosci.* **38**, 3809–3822 (2018).
18. Yan, J., Porch, M. W., Court-Vazquez, B., Bennett, M. V. L. & Zukin, R. S. Activation of autophagy rescues synaptic and cognitive deficits in fragile X mice. *Proc. Natl Acad. Sci. USA* **115**, E9707–E9716 (2018).
19. Duan, K. et al. Mitophagy in the basolateral amygdala mediates increased anxiety induced by aversive social experience. *Neuron* **109**, 3793–3809.e8 (2021).
20. Merenlender-Wagner, A. et al. Autophagy has a key role in the pathophysiology of schizophrenia. *Mol. Psychiatry* **20**, 126–132 (2015).
21. Moigneu, C. et al. Systemic GDF11 attenuates depression-like phenotype in aged mice via stimulation of neuronal autophagy. *Nat. Aging* **3**, 213–228 (2023).
22. Tang, G. et al. Loss of mTOR-dependent macroautophagy causes autistic-like synaptic pruning deficits. *Neuron* **83**, 1131–1143 (2014).
23. Tomoda, T., Yang, K. & Sawa, A. Neuronal autophagy in synaptic functions and psychiatric disorders. *Biol. Psychiatry* **87**, 787–796 (2020).
24. Gassen, N. C. et al. Association of FKBP51 with priming of autophagy pathways and mediation of antidepressant treatment response: evidence in cells, mice, and humans. *PLoS Med.* **11**, e1001755 (2014).
25. Zhang, S.-Q. et al. Cell type-specific NRBF2 orchestrates autophagic flux and adult hippocampal neurogenesis in chronic stress-induced depression. *Cell Discov.* **9**, 90 (2023).
26. Gulbins, A. et al. Antidepressants act by inducing autophagy controlled by sphingomyelin-ceramide. *Mol. Psychiatry* **23**, 2324–2346 (2018).
27. Cerniauskas, I. et al. Chronic stress induces activity, synaptic, and transcriptional remodeling of the lateral habenula associated with deficits in motivated behaviors. *Neuron* **104**, 899–915.e8 (2019).
28. Li, B. et al. Synaptic potentiation onto habenula neurons in the learned helplessness model of depression. *Nature* **470**, 535–539 (2011).
29. Zheng, Z. et al. Hypothalamus-habenula potentiation encodes chronic stress experience and drives depression onset. *Neuron* **110**, 1400–1415.e6 (2022).
30. Lecca, S. et al. Rescue of GABAB and GIRK function in the lateral habenula by protein phosphatase 2A inhibition ameliorates depression-like phenotypes in mice. *Nat. Med.* **22**, 254–261 (2016).
31. Zheng, Z. et al. A small population of stress-responsive neurons in the hypothalamus-habenula circuit mediates development of depression-like behavior in mice. *Neuron* **112**, 3924–3939.e5 (2024).
32. Huang, T. et al. Input-output specific orchestration of aversive valence in lateral habenula during stress dynamics. *J. Zhejiang Univ. Sci. B* **25**, 1055–1065 (2024).
33. Chen, M. et al. Brain region-specific action of ketamine as a rapid antidepressant. *Science* **385**, eado7010 (2024).
34. Zhu, X. et al. Distinct thalamocortical circuits underlie allodynia induced by tissue injury and by depression-like states. *Nat. Neurosci.* **24**, 542–553 (2021).
35. Yang, Y. et al. Ketamine blocks bursting in the lateral habenula to rapidly relieve depression. *Nature* **554**, 317–322 (2018).
36. Li, L. et al. Social trauma engages lateral septum circuitry to occlude social reward. *Nature* **613**, 696–703 (2023).
37. Mizushima, N., Yamamoto, A., Matsui, M., Yoshimori, T. & Ohsumi, Y. In vivo analysis of autophagy in response to nutrient starvation using transgenic mice expressing a fluorescent autophagosome marker. *Mol. Biol. Cell* **15**, 1101–1111 (2004).
38. Cui, Y. et al. Astroglial Kir4.1 in the lateral habenula drives neuronal bursts in depression. *Nature* **554**, 323–327 (2018).
39. Rosenkranz, J. A., Venheim, E. R. & Padival, M. Chronic stress causes amygdala hyperexcitability in rodents. *Biol. Psychiatry* **67**, 1128–1136 (2010).
40. Fang, X. Increased intrinsic and synaptic excitability of hypothalamic POMC neurons underlies chronic stress-induced behavioral deficits. *Mol. Psychiatry* **28**, 1365–1382 (2023).
41. Lieberman, O. J. et al. Cell-type-specific regulation of neuronal intrinsic excitability by macroautophagy. *eLife* **9**, e50843 (2020).
42. Selye, H. A syndrome produced by diverse noxious agents. *Nature* **138**, 32–32 (1936).
43. Kallergi, E. et al. Profiling of purified autophagic vesicle degradome in the maturing and aging brain. *Neuron* **111**, 2329–2347.e7 (2023).
44. Abdallah, C. G. et al. Modulation of the antidepressant effects of ketamine by the mTORC1 inhibitor rapamycin. *Neuropsychopharmacology* **45**, 990–997 (2020).
45. Cleary, C. et al. Antidepressive-like effects of rapamycin in animal models: Implications for mTOR inhibition as a new target for treatment of affective disorders. *Brain Res. Bull.* **76**, 469–473 (2008).
46. Duman, R. S., Sanacora, G. & Krystal, J. H. Altered connectivity in depression: GABA and glutamate neurotransmitter deficits and reversal by novel treatments. *Neuron* **102**, 75–90 (2019).
47. Casarotto, P. C. et al. Antidepressant drugs act by directly binding to TRKB neurotrophin receptors. *Cell* **184**, 1299–1313.e19 (2021).
48. Wang, C. S., Kavalali, E. T. & Monteggia, L. M. BDNF signaling in context: from synaptic regulation to psychiatric disorders. *Cell* **185**, 62–76 (2022).
49. Lei, T. et al. Risperidone treatment in the lateral habenula improves despair-like behavior in mice. *Neuropsychopharmacology* **45**, 1717–1724 (2020).

Publisher's note Springer Nature remains neutral with regard to jurisdictional claims in published maps and institutional affiliations.



Open Access This article is licensed under a Creative Commons Attribution-NonCommercial-NoDerivatives 4.0 International License, which permits any non-commercial use, sharing, distribution and reproduction in any medium or format, as long as you give appropriate credit to the original author(s) and the source, provide a link to the Creative Commons licence, and indicate if you modified the licensed material. You do not have permission under this licence to share adapted material derived from this article or parts of it. The images or other third party material in this article are included in the article's Creative Commons licence, unless indicated otherwise in a credit line to the material. If material is not included in the article's Creative Commons licence and your intended use is not permitted by statutory regulation or exceeds the permitted use, you will need to obtain permission directly from the copyright holder. To view a copy of this licence, visit <http://creativecommons.org/licenses/by-nc-nd/4.0/>.

© The Author(s) 2025, corrected publication 2025

Article

Methods

Animals and ethical approval

All mice (aged 7–15 weeks, if not specified) were bred in our colony (that is, *Atg7^{lox/lox}* lines⁵⁰ and GFP-LC3 lines) or purchased from SLAC (that is, C57BL/6j and CD-1 mice). CD-1 mice (4–6 months old, retired breeders) were single-housed, and all other mice were housed 4–5 per cage if not specified. All animals were subjected to a 12-h light–dark cycle (light on from 7:00 to 19:00) with food and water ad libitum. All mice were housed in a stable environment (23–25 °C ambient temperature and around 50% humidity). Only male mice were used in this study. All animal research and experimental procedures were approved by the Animal Care and Use Committee of the animal facility at Zhejiang University.

Bulk RNA-seq

RNA-seq was performed with fresh LHb, vHippo, mPFC, VTA, lateral hypothalamus and NAc samples from CRS and naive mice tested using FST 2 days before euthanasia. We divided CRS and naive mice into two groups, respectively. Namely CRS mice with high FST scores (FST immobility for more than 110 s, $n = 3$), CRS mice with low FST scores (50 s less than FST immobility less than 110 s, $n = 3$), naive mice with high FST scores (50 s less than FST immobility less than 80 s, $n = 3$), naive mice with low FST scores (FST immobility less than 50 s, $n = 3$). On the third day, mice were euthanized after anaesthesia with 1% pentobarbital NEMBUTAL (100 mg kg⁻¹) and perfused with 20 ml of ice-cold phosphate-buffered saline (PBS, pH 7.4). The brains were collected quickly on an ice plate and moved to liquid nitrogen for 25 s. Frozen brains were fitted into stainless steel mouse brain matrices and sectioned with blades into roughly 1-mm coronal slices containing the LHb (–1.5 to –1.9 mm from bregma), vHippo (–2.9 to –3.3 mm from bregma), mPFC (+1.9 to +1.5 mm from bregma), VTA (–2.9 to –3.3 mm from bregma), lateral hypothalamus (–0.6 to –1.0 mm from bregma) and NAc (+1.3 to +0.9 mm from bregma). Slices were immersed in ice-cold PBS and relevant brain regions were carefully micro-dissected on an ice plate under microscope. The samples were put into a marked Eppendorf tube and were then quickly transported into liquid nitrogen for subsequent mRNA sequencing under customized service of LC-Bio Technology. After the final transcriptome was generated, StringTie and ballgown were used to estimate the expression levels of all transcripts and determine mRNA expression abundance by calculating the FPKM value. Genes differential expression analysis was performed by DESeq2 software. The genes with $P < 0.05$ and absolute fold change greater than or equal to 1.2 were considered differentially expressed genes. Differentially expressed genes were then subjected to enrichment analysis of KEGG pathways. z -score values stand for the up- or downregulation of all genes enriched to this pathway. Bioinformatic analysis was performed using the OmicStudio tools at <https://www.omicstudio.cn/tool>. KEGG analysis and statistics of mRNA expression level were compared only between CRS mice with high FST scores and naive mice with low FST scores. For correlation analysis, all mice were included.

snRNA-seq

The LHb from CRS and naive mice was transferred to tissue storage solution (130-100-008, Miltenyi), and the suspension after filtration, centrifugation and resuspension was loaded onto the Chromium single-cell controller (10X Genomics) to generate single-cell gel beads in the emulsion according to the manufacturer's protocol by LC-Bio Technology. Postprocessing and quality control were carried out by 10X Cell Ranger package (v.1.2.0, 10X Genomics). The bioinformatics analysis of snRNA-seq was conducted by LC-Bio Technology. Clustering analysis was carried out with standard *seurat* package procedures at a resolution of 1.20. The clusters were then assigned to neuronal and glial cell types by their canonical gene markers. *Syp* marked neuron clusters, *Mag* marked oligodendrocyte clusters, *Gja1* marked astrocyte clusters

and *C1qc* marked microglia clusters. To further explain differentially expressed autophagy-related genes among these cell types, we used gene set variation analysis to analyse the 'Autophagosome Formation' pathway.

Western blotting

Samples were collected using the same protocol as described in 'Bulk RNA-seq'. After micro-dissection, LHb (–1.5 to –1.9 mm from bregma), vHippo (–2.9 to –3.3 mm from bregma), mPFC (+1.9 to +1.5 mm from bregma), VTA (–2.9 to –3.3 mm from bregma), lateral hypothalamus (–0.6 to –1.0 mm from bregma) and NAc (+1.3 to +0.9 mm from bregma), lateral septum (+0.9 to +0.5 mm from bregma), dorsal raphe nucleus (–4.2 to –4.6 mm from bregma), median raphe nucleus (–4.2 to –4.6 mm from bregma), arc (–1.2 to –1.5 mm from bregma), BLA (–1.3 to –1.9 mm from bregma) and liver samples were transferred to ice-cold lysis buffer (0.32 M sucrose, 10 mM HEPES pH 7.4, 2 mM EDTA, 1 mM PMSF, 1× Protease inhibitors, 1× Phosphatase inhibitors) and homogenized using ultrasonic cell grinder. Part of the lysates were taken as a total protein sample and incubated for 30 min on ice with 10% SDS. Remaining lysates were centrifuged at 1,000g for 10 min to remove pelleted nuclear fraction. The supernatant was then taken and centrifuged again at 15,000g for 30 min. The new supernatant was discarded and the pellet was resuspended in RIPA buffer (50 mM Tris pH 7.4, 150 mM NaCl, 1% Triton X-100, 1% sodium deoxycholate, 0.1% SDS, 1 mM PMSF, 1× Protease inhibitors, 1× Phosphatase inhibitors) as crude synaptosome sample that would be subsequently incubated on ice for 30 min. Samples were diluted in 5× SDS–PAGE loading buffer and were boiled at 95 °C for 5 min. Next, the samples were loaded on an SDS (8–15%) polyacrylamide gradient gel and transferred onto a polyvinylidene difluoride membrane. The blots were incubated at 4 °C overnight with one of the following primary antibodies: rabbit anti-p62 (1:2,000, PM045, MBL), rabbit anti-Beclin-1 (1:1,000, 3495, CST), mouse anti-Atg7 (1:1,000, 67341-1-Ig, Proteintech), mouse anti-ubiquitin (1:1,000, 3936, CST), rabbit anti-p-AMPA α (Thr172) (1:1,000, 2535, CST), rabbit anti-p-mTOR (1:1,000, ab137133, Abcam), rabbit anti-p-p70S6 Kinase 1-T421/S424 (1:1,000, APO502, Abclonal), rabbit anti-p-Akt (1:1,000, 4058, CST), rabbit anti-Cleaved Caspase-3 (1:1,000, 9664, CST), rabbit anti-GluA1 (1:1,000, ab31232, Abcam), rabbit anti-GluA2 (1:1,000, 11994-1-AP, Proteintech), rabbit anti-GluN1 (1:1,000, ab109182, Abcam), rabbit Anti-GABA_A Receptor alpha 1 (1:1,000, ab252430, Abcam), mouse anti- β -actin (1:5,000, MAS-15739, Thermo Fisher Scientific) or rabbit anti- α -tubulin (1:2,000, 11224-1-AP, Proteintech). The next day, horseradish peroxidase (HRP)-conjugated secondary antibodies, including anti-mouse IgG, HRP-linked antibody (1:10,000, 31430, Thermo Fisher Scientific) and anti-rabbit IgG, HRP-linked antibody (1:5,000, 31460, Thermo Fisher Scientific) were revealed using an ECL kit (Immobilon Ultra Western HRP Substrate, MILLIPORE) for protein detection. Selected films were scanned and quantified using BioRad Image Lab software (v.6.0). Some blots then were incubated in stripping buffer (Beyotime) for 20 min at room temperature followed by three washes with tris-buffered saline with Tween. After being reblocked, membranes were re-incubated with another primary antibody overnight at 4 °C. The following steps were the same as described above. β -actin and α -tubulin bands were used for normalization.

For gel source data, see the Supplementary Information.

Immunohistochemistry

Mice (7–8 weeks) that experienced ARS or CRS were anaesthetized and perfused with 20 ml of PBS followed by 20 ml of 4% paraformaldehyde (PFA) in PBS. After decapitation, brains were dissected and transferred to 4% PFA for postfixation for 24 h at 4 °C. The fixed brains were then dehydrated in 30% sucrose in PBS at 4 °C for 24 h and sectioned into 20- μ m sections with a microtome (Thermo Scientific, NX50). Free-floating slices were washed three times in PBS, then moved onto microscope slides and permeabilized with 0.5% Triton X-100 in PBS for

20 min at room temperature. Slices were rinsed three times and then preserved in blocking buffer (5% normal goat serum) for 1 h at room temperature. Some sections were incubated with primary antibodies (mouse anti-LC3, 1:200, A17424, ABclonal; or rabbit anti-NeuN, 1:500, A19086, ABclonal) for 24 h at 4 °C to stain LC3 and NeuN, and other sections were incubated with primary antibodies (rabbit anti-LC3, 1:1,000, ab192890, Abcam; mouse anti-PSD95, 1:500, ab13552, Abcam; or guinea pig anti-NeuN, 1:500, ABN90, Sigma-Aldrich) for 48 h at 4 °C to stain LC3, PSD95 and NeuN. These were then rinsed three times with PBS and incubated with secondary antibodies for 1 h at room temperature (goat anti-mouse, 1:100, ASO08, ABclonal or 1:1,000, A-21235, Thermo Fisher Scientific; goat anti-rabbit, 1:1,000, AS060, ABclonal, or 1:1,000, A-11008, Thermo Fisher Scientific; goat anti-guinea pig, 1:1,000, A-21435, Thermo Fisher Scientific) and finally rinsed again three times with PBS. For GFP-LC3 mice, 4,6-diamidino-2-phenylindole (DAPI) staining was applied for visualization of cells. Fluorescent image acquisition was performed with Leica SP8 Laser confocal microscope. Three slices (anterior, middle and posterior) and two views of each hemisphere of LHB were selected for counting. Confocal z-stack images were collapsed using the Z Projection-Max intensity function in Image J. LC3 puncta positive neurons were counted manually.

RNA isolation and real-time qPCR

Immediately after dissection, RNA was extracted using RNeasy Kit (AC0202-B, Shandong Sparkjade Biotechnology) according to the instruction protocol. Following extraction, RNA quality was evaluated by measuring the absorption at 230, 260 and 280 nm by the Nano Drop 2000 Spectrophotometer (Thermo Scientific). A ratio of A260/A280 = 1.8/2.1 was considered high purity. Complementary DNA (cDNA) synthesis was done using cDNA Synthesis Kit (R323-01, Vazyme), which was then used as a template for real-time qPCR. Real-time qPCR was carried out in a LightCycler 96 (Roche) using SYBR Green Pro Taq HS (AG11701, ACCURATE BIOTECHNOLOGY) according to the standard protocols. Melting curve analysis was performed to ensure a single peak for each PCR product. The gene expression levels were normalized by the average levels of *Actb*. All measurements were performed in triplicate and analysed using the $2^{-\Delta\Delta Ct}$ method. Primers (5'–3') used were as follows: *Actb*, GACGGCC AGGTCATCACTATTG and AGGAAGGCTGAAAAGAGCC; *Atg7*, GCTG CTGAGATCTGGGACAT and GAGATGTGGAGATCAGGACCAG; *Atg10*, AGGTCAGGGCGAGCGA and CCATCGCCTATCTGCTGTGA; *Atg5*, TGTG CTTCGAGATGTGTGGTT and GTCAAATAGCTGACTCTTGGCAA; *Atg4d*, CCCCggcattcactgtactt and TGGCAAAGGCCATCTCCAG; *Atg12*, TGAATCAGTCCTTTGCCCTand CATGCCTGGGATTTGCCAG; *Becn1*, ATACTGTTCTGGGGGTTTCCG and GTCTCTCCTTTTTCCACC TCTTC; *LC3*, TTATAGACGATACAAGGGGGAG and CGCCGTCTGATT ATCTTGATGAG; *Mtor*, CAGACTGGCTCTTGTCTATAA and GCTGGAAG GCGTCAATC; *AMPK*, GTCAAAGCCGACCCAATGATA and CGTACACG AATAATAGGGGTT.

Electron microscopy

Mice were anaesthetized with 1% Pentobarbital NEMBUTAL (100 mg kg⁻¹, Sigma-Aldrich) and perfused with 4% PFA in PBS. The brains were collected quickly and fitted into stainless steel mouse brain matrices and sectioned with blades into roughly 1-mm coronal slices containing the LHB (-1.5 to -1.9 mm from bregma). The LHB samples were postfixed with 2.5% glutaraldehyde in 0.1 M PBS (pH 7.4) for 12 h at 4 °C. Samples were then washed three times (10 min each) in 0.1 M PBS, treated with 1% OsO₄ in 0.1 M PBS for 40 min and washed three times (10 min each) in ddH₂O. Slices were then treated with 2% uranyl acetate in ddH₂O for 30 min. Finally, sections were successively dehydrated in 50, 70 and 90% ethanol (15 min each), then 100% ethanol (20 min each), followed by 100% acetone twice (20 min each). Sections were embedded in EPON resin and sliced into sections at 85 nm thickness. We inspected 15 random neurons (Thermo Scientific Talos L120C Electron Microscopy) and

manually counted the autophagosomes, which are distinguished from other organelles by their oval or round shapes and double-membrane structures^{8,37}.

Immunoelectron microscopy

Mice were anaesthetized with 1% Pentobarbital NEMBUTAL (100 mg kg⁻¹, Sigma-Aldrich) and perfused with 4% PFA and 0.1% glutaraldehyde in 0.1 M phosphate buffer. The brains were removed quickly and fixed in the same fixative overnight at 4 °C. Fixed brains were then cut into 50- μ m sections using a Leica VT1200S vibratome and the slides were kept in the same fixative for 2 h at room temperature. Free-floating 50- μ m brain sections were collected and washed three times (15 min each) in phosphate buffer. To eliminate unbound aldehydes, sections were incubated in 50 mM glycine for 30 min, then rinsed with phosphate buffer for 15 min. The brain slides were permeabilized by 0.05% Triton X-100 in phosphate buffer for 15 min, and washed for another 15 min in phosphate buffer. The slides were incubated in 0.1% BSA-cold water fish gelatin (Ctm) in PBS for 30 min. Subsequently, primary antibody was then added with incubation buffer and slides were left for 1 h at room temperature, followed by an overnight incubation with primary antibody (rabbit anti-GluA2 1:100, 11994-1-AP, Proteintech) at 4 °C. The following day, slides were washed six times (10 min) with 0.1% BSA-Ctm in PBS. The slides were then incubated with Nanogold-labelled Fab' goat anti-rabbit (1:50, N-24916, Thermo Fisher Scientific) for 1 h at room temperature, adjusted to 4 °C overnight. On the fourth day, slides were washed six times (10 min) with 0.1% BSA-Ctm in PBS and washed twice (10 min) in phosphate buffer. The slides were fixed again with 2.5% glutaraldehyde in phosphate buffer for 2 h and washed three times (10 min) in phosphate buffer. The slides were washed six times (5 min) in ddH₂O thoroughly. For silver using nanogold, slides were washed three times (5 min) in 0.02 M sodium citrate buffer and then underwent silver enhancement (HQ silver enhancement kit, Nanoprobes). After silver enhancement, the slides were washed six times (10 min) thoroughly with ddH₂O and incubated in ddH₂O overnight at 4 °C. On the fifth day, slides were washed three times (10 min) in PBS and placed in 1% OsO₄ for 40 min. The slides were then washed three times (10 min) with ddH₂O and placed in 2% Uranyl acetate for 30 min. Finally, the slides were washed three times (10 min) again, and were dehydrated with ethanol, 50% ethanol for 15 min, 70% ethanol for 15 min, 90% ethanol for 15 min, 100% ethanol twice (20 min), followed by 100% acetone twice (20 min). After incubation in EPON 812 mixed with acetone (1:1) for 2 h, the slides were embedded in EPON, and regions of interest were sectioned at 90 nm using an ultramicrotome (LEICA EM UC7). The slices were observed and photographed using transmission electron microscopy (Tecnai Spirit Bio-Twin) with an accelerating voltage of 120 kV, charge-couple device camera (Gatan, 15081901W0832) at the Center of CyroElectron microscopy, Zhejiang University. Quantitative analyses were performed to establish degree of GluA2 immunoreactivity colocalized within autophagosomes (quantified from 15 randomly selected neurons) in LHB from mice treated with ARS or CRS.

STORM

Four weeks after adeno-associated virus (AAV)-mCherry-EGFP-LC3 injection surgery, mice with or without surgery were restrained in 50-ml conical tubes for 2 h. They were then anaesthetized immediately and perfused with PBS followed by 4% PFA in PBS. The brains were dissected, postfixed in 4% PFA at 4 °C for 24 h, and then dehydrated in 30% sucrose in PBS for 48 h. Brains were sectioned into 20- μ m slices using a microtome (Thermo Scientific NX50) and preserved in PBS. Free-floating slices were preserved in blocking buffer (5% normal goat serum and 0.3% Triton X-100 in PBS) for 1 h at room temperature. Slices were then incubated with primary antibodies (rabbit anti-GluA2, 1:250, 11994-1-AP, Proteintech, with or without mouse anti-LC3, 1:100, 83506, CST) in antibody dilution (5% normal goat serum, 0.3% Triton X-100, 1% bovine serum albumin in PBS) overnight at 4 °C. Slices were then

Article

washed with PBS (three times for 10 min) and incubated with secondary antibodies (goat anti-rabbit, 1:1,000, AS060, ABclonal, with or without goat anti-mouse, 1:1,000, A11001, Invitrogen) in antibody dilution for 2 h at room temperature. Finally, slices were washed with PBS (3 × 10 min) and incubated for 30 min at room temperature. The slice was immersed into STORM imaging buffer and LHB, Arc and BLA were immediately imaged with a Nikon N-STORM super-resolution system (Nikon Instruments) equipped with a ×100 oil immersion objective (CFI Apo ×100 oil, numerical aperture 1.49, TIRF WD 0.12) and Andor camera (Ixon 897 back-illuminated EMCCD). The buffer was freshly prepared before imaging and contained 7 μl of oxygen-scavenging GLOX buffer (14 mg glucose oxidase, 50 μl of 17 mg ml⁻¹ catalase in 200 μl of 10 mM Tris and 50 mM NaCl, pH 8.0), 35 μl of 1 M MEA buffer, and 7 μl of β-mercaptoethanol. A conventional wide-field fluorescence image was acquired with low laser power to identify the imaging objects and focal plane. The 647, 561 and 488 nm laser was turned to maximum power to turn off the fluorophores and trigger photo-switching. Nikon NIS Element v.4.51 software was used to perform three-dimensional reconstruction.

TUNEL assay

Three weeks after AAV-hSyn-mCherry-2A-Cre or AAV2/9-hSyn-MCS-mCherry-3×Flag injection surgery, mice were anaesthetized and perfused with PBS followed by 4% PFA in PBS. The brains were dissected, postfixed in 4% PFA at 4 °C for 24 h, and then dehydrated in 30% sucrose in PBS for 48 h. Brains were subsequently sliced into 50-μm sections. Terminal deoxynucleotidyl transferase (TdT)-mediated deoxyuridine triphosphate nick end labelling (TUNEL) assay was performed with the TUNEL Apoptosis Detection Kit (40307ESS0, Yeasen) according to the manufacturer's instructions. Brain slices were rinsed twice with PBS (15 min each), followed by treatment with 100 μl of Proteinase K solution (20 μg ml⁻¹) at room temperature for 40 min, and then washed three times (5 min each) with PBS. For positive controls, each slice was incubated in 100 μl of 1× DNase I Buffer and 100 μl of DNase I (10 U ml⁻¹) for 5 min and 10 min, respectively, then washed three times (5 min each) with dH₂O. All slices were further equilibrated in 100 μl of 1× equilibration buffer at room temperature for 15 min and treated with 50 μl of TdT incubation buffer (34 μl of ddH₂O, 10 μl of 5× equilibration buffer, 5 μl of Alexa Fluor 488-12-dUTP Labelling Mix, 1 μl of Recombinant TdT Enzyme) at 37 °C for 1 h. Subsequently, the slices were washed five times (5 min each), first with PBS, then with 0.1% Triton X-100 in PBS and finally with PBS three times. DAPI staining solution (Solarbio) was used to visualize nuclei. Fluorescent images were acquired with an Olympus Slideview VS200 microscope and Olympus Fluoview FV3000 confocal microscope. The TUNEL signals (TUNEL/AAV virus/DAPI colabelled) and virus-infected neurons (AAV virus/DAPI colabelled) were counted manually with Fiji (v.2.1.0/1.53 c) within the LHB.

Viral vectors

AAV2/9-hSyn-oChIEF-tdTomato (titre 1.52 × 10¹³ vector genomes (v.g.) ml⁻¹, Taitool Bioscience), AAV2/9-hSyn-mCherry-2A-Cre (titre 4.71 × 10¹³ v.g. ml⁻¹, OBio Technology), AAV2/9-hSyn-shRNA-*Atg5*-Zs Green (titre 1.7 × 10¹² v.g. ml⁻¹, Hanbio), AAV2/9-hEF1α-DIO-hM4Di-mCherry (titre 1.35 × 10¹³ v.g. ml⁻¹, Taitool Bioscience), AAV2/9-hEF1α-DIO-mCherry (titre 1.25 × 10¹³ v.g. ml⁻¹, Taitool Bioscience), AAV2/9-EF1α-DIO-GCaMP6s (titre 5.94 × 10¹³ v.g. ml⁻¹, OBio Technology), AAV2/9-hSyn-GCaMP6s (titre 1.67 × 10¹³ v.g. ml⁻¹, Taitool Bioscience), AAV2/9-hSyn-MCS-mCherry (titre 5.00 × 10¹³ v.g. ml⁻¹, OBio Technology) were diluted to 1.00 × 10¹² v.g. ml⁻¹. AAV2/5-hSyn-shRNA-*Atg7*-EGFP (titre 5.47 × 10¹³ v.g. ml⁻¹, Sunbio Medical Biotechnology), AAV2/5-hSyn-EGFP (titre 7.8 × 10¹³ v.g. ml⁻¹, Sunbio Medical Biotechnology), AAV2/5-hSyn-shRNA-BECN1-mCherry (titre 3.67 × 10¹³ v.g. ml⁻¹, Sunbio Medical Biotechnology), AAV2/9-CMV-mCherry-EGFP-LC3 (titre 1 × 10¹³ v.g. ml⁻¹, Hanbio) were diluted to 5.00 × 10¹² v.g. ml⁻¹. AAV2/9-hSyn-Cre-EGFP (titre 1.67 × 10¹³ v.g. ml⁻¹, Taitool Bioscience)

were diluted to 5.00 × 10¹¹ v.g. ml⁻¹. The cholera toxin subunit B (CTB-647) (0.2%, Invitrogen) was dissolved in PBS.

Stereotaxic surgery, virus injection and optic fibre and/or cannula implantations

For stereotaxic surgery, C57BL/6J mice or *Atg7^{fllox/fllox}* mice (7–8 weeks) were anaesthetized. Viruses were bilaterally injected with a glass pipette mounted on a stereotaxic frame into one of the following brain regions: LHB (±0.46 mm medial–lateral, –1.72 mm anterior–posterior from bregma, –2.70 mm dorsal–ventral from the dura), vHippo (±2.80 mm medial–lateral, –3.0 mm anterior–posterior from bregma, –3.80 mm dorsal–ventral from the dura), lateral hypothalamus (±1.00 mm medial–lateral, –0.75 mm anterior–posterior from bregma, –4.78 mm dorsal–ventral from the dura). Volumes of virus or CTB ranged between 100 and 200 nl per hemisphere, infused at a rate of 100–150 nl min⁻¹. Injection pipette was withdrawn from the brain 10 min after the infusion. After surgery, mice were placed on a heating pad to recover from anaesthesia.

For optic fibre implantation, optic fibres (200-μm diameter, 0.37 numerical aperture, Inper Ltd) were bilaterally implanted 250 μm above the viral injection site and cemented onto the skull using dental cement. Viral expression profiles were verified by histology after completion of all experiments as shown in Extended Data Fig. 6h–k.

For cannulae implantation, a double guide cannulae (side-by-side distance 1.0 mm, RWD) was implanted bilaterally over the LHB (±0.46 mm mediolateral; –1.72 mm anterior–posterior from bregma and –2.20 mm dorsoventral from the dura) of C57BL/6J mice.

Cannula infusion experiment

For cannula implantation, a double guide cannulae was implanted over the bilateral LHB. tBP, Dyngo-4a, tBP with Dyngo-4a or TAT-GluA_{2,3y}, or vehicle was microinjected into the LHB 30 min before each behavioural test. For sustained effect test, behavioural tests were conducted at 24 h, on the seventh, 18th and 19th days following tBP infusion into the LHB of CRS mice. For prophylactic effect test, local tBP infusions occurred before the first, fifth and ninth days of restraint during 14-day CRS. SBI or vehicle was microinjected into the LHB before ARS. The double injector cannulae were connected with the micro-syringe using a polyethylene pipe filled with mineral oil. tBP (Selleck, 20 μg μl⁻¹, ref. 12) was dissolved in saline, and SBI (MCE, 5 μM) was dissolved in 10% DMSO, 40% PEG300, 5% Tween-80 and 45% saline. For all cannula infusion experiments, 150 nl of each drug was infused into the LHB bilaterally through the double injector cannulae. The injector cannulae were left in the LHB for an extra 4–5 min to allow adequate local drug diffusion and minimize the spread of the drug along the cannula track. The drug infusion sites were verified after all behavioural tests with CTB-647 (150 nl per side) injected into both sides of the LHB. Fluorescent image acquisition was performed with an Olympus Slideview VS200 microscope slide scanning system. Data were used only from mice with accurate injection sites.

Optogenetic manipulation

A blue light laser of 465-nm intensity was delivered at 5 mW, 2-ms pulse width. Mice were placed in the home cage and received 40 Hz phasic photostimulation as previously described²⁹ (40 Hz, five pulses per second, 10 min at intervals of 5 min, a total of 2 h) or LFS protocol (1 Hz, 15 min).

Intraperitoneal injection

Paroxetine-HCl (APE×BIO, 5 mg kg⁻¹) was dissolved in saline. For acute experiment, CRS mice were injected with paroxetine-HCl or vehicle 1 day before euthanasia or behavioural tests. For the chronic experiment, CRS mice were injected with paroxetine-HCl or vehicle for seven consecutive days and euthanized the next day, whereas *Atg7^{LHB-/-}* or *Atg7^{LHB+/-}* mice with CRS were injected with paroxetine-HCl or vehicle

for seven consecutive days before behavioural tests. For the ketamine experiment, CRS mice were injected with ketamine (Drug reference materials laboratory of the Third Research Institute of Ministry of Public Security, 10 mg kg⁻¹) or vehicle 1 or 24 h before euthanasia, and *Atg7^{LHb-/-}* mice were injected with ketamine or vehicle 24 h before behavioural tests. Rapamycin (MCE, 10 mg kg⁻¹) was dissolved in 10% DMSO, 40% PEG300, 5% Tween-80 and 45% saline. For behavioural tests and western blot, rapamycin or vehicle were injected for three consecutive days, and an extra 1 h before euthanasia or behavioural test.

Behavioural assays

All behavioural tests were conducted in a sound attenuation room to minimize external auditory stimuli.

Restraint stress

Mice were placed in 50-ml conical tubes that were drilled with several small holes (2 mm in diameter) for ventilation and were subjected to ARS (2 h) or CRS (2 h of restraint stress for 14 consecutive days). During fibre photometry, each mouse was gently grasped by one of the experimenter's hands that was wearing a cotton glove for 10 s, and the tail was immobilized with the other hand²⁹.

Social defeat stress

As previously described^{29,36}, CD-1 aggressors were screened for aggressive behaviours towards intruders. Mice were placed in the home cage of a CD-1 aggressor and attacked for 5–10 min and then housed with the aggressor for 24 h, separated by a perforated transparent partition in the middle of the cage. Chronic social defeat stress lasted for ten consecutive days and mice were exposed to a new aggressor each day. For fibre photometry recording, tested mice were recorded during the 5 min of social defeat stress.

Footshock stress

As previously described^{29,30}, mice were placed in a shock box and allowed to freely explore the box for 5 min. Electrical footshocks (0.8 mA, 1–3 s duration) were then delivered at random intervals (1–15 s). Chronic footshock stress consisted of 360 footshocks within 60 min and was given for two consecutive days. For acute footshock stress, mice were subjected to 15 random footshocks within 3 min. For fibre photometry, mice were recorded during the footshock stress.

FST

Mice were gently and individually placed in a cylinder (12 cm in diameter and 25 cm in height) filled with water (23–25 °C) and allowed to swim for 6 min under normal illuminating conditions. The depth of water was adjusted to prevent the mice from touching the bottom of the cylinder with their hind limbs or tails. The behaviour of the mice was videotaped from the side. The immobile duration within the last 4 min was analysed by an experimenter blinded to the animal treatments. Immobility was defined as a state in which the mice remained floating with only necessary movements to keep balance in the water.

SPT

Mice were single housed followed by 2 days of adaptation with two bottles of water, after which mice were water deprived for 24 h before the test. During the test, mice were given one bottle of water and one bottle of 1% sucrose solution. Acute SPT was measured for the first 3 h in the active phase of mice, with the positions of the two bottles switched every 0.5 h to eliminate any baseline place preference. The consumption of water and sucrose was recorded by an experimenter blinded to the animal treatments. Sucrose preference was defined by the average percentage of sucrose consumption relative to total fluid consumption in 3 h. For chronic SPT, the sucrose consumption percentage was continuously monitored for the next 2 days, while the bottle positions were switched at the light phase and consumption was

measured every 12 h to ensure balanced measurements across different positions and phases.

OFT

OFT was conducted before all other behavioural tests. The mice were gently placed in the centre of a square arena (40 × 40 × 40.5 cm), with the illumination above the centre brighter than the peripheral area. A video camera positioned directly above the arena was used to track the movement of each mouse by means of Any-maze software (Stoelting).

SIT

An OFT box containing a wire-mesh cage was used on one side. Video tracking software (Any-maze, Stoelting) was used to measure the amount of time the experimental mouse spent in the social interaction zone (15 × 15 cm) surrounding the wire-mesh cage within the arena. The open field arena and wire-mesh enclosures were thoroughly cleaned between each experimental mouse. Mice were individually placed in the centre of the OFT box and allowed to explore freely for 2.5 min (without social target present, known as the 'no target' phase). The experimental mouse was then removed, an unfamiliar c57 mouse was placed under the mesh cage (known as the 'target' phase). The experimental mouse was then returned to the OFT box and allowed to explore for another 2.5 min, during which time spent interacting with the social target was measured. The social interaction (SI) ratio was calculated as: SI ratio = ((time in SI zone in target phase)/(time in SI zone in no target phase)) × 100.

Fibre photometry

Following 3–5 weeks of viral expression, GCaMP6s fluorescence was detected using a fibre photometry system (Inper Ltd). The Ca²⁺-dependent signal was detected by a 470-nm LED (20 μW) whereas the Ca²⁺-independent isosbestic signal was detected by a 410-nm LED (20 μW). A video camera (PHILIPS, p506) was installed above the centre of the arena to record the behaviours of tested mice. We applied a screen recorder to synchronize behavioural events and fluorescence signals (EV Capture). All mice expressing GCaMP6s were allowed to accommodate to the new environment for at least 1 hr before the recording sessions. When mice were quiet but stayed alert, a 10-min baseline was recorded. After that, each mouse was exposed to acute stressors and their neuronal Ca²⁺ responses were recorded.

Fibre photometry data analysis

To calculate the change ratios of the fluorescence, raw data were analysed by using a processing software (Inper Ltd) and MATLAB code (Thinker Tech Nanjing Biotech). We segmented the photometry data based on specific behavioural events within individual trials. Movement artefacts were corrected by recording the fluorescent signal that is stimulated with a 410-nm LED. This signal elicited by the 410-nm LED was linearly scaled using least-squares regression to minimize the difference between signals elicited by the 410- and 470-nm LEDs. We then subtracted the scaled 410-nm signal from the 470-nm signal to exclude the movement artefacts and obtain bleaching-corrected signals. We defined the change ratios of fluorescence ($\Delta F/F_0$) by calculating $(F - F_0)/F_0$, in which F_0 was the averaged value of baseline fluorescence signals recorded before acute stress. $\Delta F/F$ ratio was presented with heat maps or as average plots with a shaded area indicating the standard error of the mean. We also calculated the area under the curve for each trial to compare the baseline response (–2–0 s) with the response to stress (0–5 s).

Slice preparation

The animals were anaesthetized with 1% pentobarbital NEMBTAL (100 mg kg⁻¹) and then perfused with 20 ml of ice-cold cutting solution (oxygenated with 95% O₂ and 5% CO₂), a modified ACSF

Article

containing 210 mM sucrose, 125 mM NaCl, 2.5 mM KCl, 25 mM NaHCO₃, 1.25 mM NaH₂PO₄, 1 mM MgCl₂, 1 mM CaCl₂, 25 mM glucose and 1 mM sodium pyruvate. After decapitation, the brains were dissected rapidly and transferred to ice-cold oxygenated cutting solution. Lhb-containing coronal slices (300- μ m thickness) were cut in ice-cold oxygenated cutting solution with a Leica VT1200S vibratome and then incubated in a recovery chamber containing normal incubation ACSF (125 mM NaCl, 2.5 mM KCl, 25 mM NaHCO₃, 1.25 mM NaH₂PO₄, 1 mM MgCl₂, 1 mM CaCl₂, 25 mM glucose) at 32 °C. Incubation ACSF was continuously bubbled with a gas mixture of 95% O₂ and 5% CO₂. Slices were allowed to recover for at least 1 h and then incubated at room temperature before electrophysiology recordings.

In vitro electrophysiology

Whole-cell patch-clamp recordings were performed on Lhb neurons at 30 °C, which was monitored with an automatic temperature controller (TC-324C, Warner Instruments). Slices were continuously perfused with ACSF (same as the incubation solution) at 2–3 ml min⁻¹. The patch pipettes (5–6 M Ω) were pulled with a pipette puller (PC-100, Narishige) from borosilicate glass (Sutter Instrument). For all whole-cell patch recordings, the pipettes were filled with an internal solution containing 127 mM K-gluconate, 13 mM KCl, 4 mM Mg₃-ATP, 0.3 mM Na₃-GTP, 0.3 mM EGTA, 10 mM HEPES and 10 mM Na-phosphocreatine (pH 7.25). Recordings were performed with a MultiClamp 700B amplifier and pCLAMP v.10.6 software (Axon Instruments). Signals were amplified, and then filtered at 2 kHz and sampled at 10 kHz using a Digidata 1550B. The series resistance and capacitance were compensated automatically after a stable giga-seal. Cells were discarded if their series resistances changed more than 20%.

To record sEPSCs and sIPSCs, neurons were held at –50 mV in a voltage-clamp mode. To record spontaneous neuronal activity, neurons were held under current clamp ($I = 0$ pA). The excitability was measured by action potentials elicited by injecting a series of current pulses (500-ms duration, –100 to 150-pA intensity with an increment of 10 or 20 pA) under current clamp.

For plasticity experiments, repetitive control photostimulation (465-nm light laser, 5 mW) was applied at 0.1 Hz to induce evoked excitatory postsynaptic currents (EPSCs). LFS protocol (1 Hz, 15 min) was used for LTD induction, whereas the excitatory postsynaptic potentials (EPSPs)-burst dependent plasticity (EBDP) protocol (4–5 pulses per second, 40 Hz, 100 stimuli for 100 s) was performed to trigger LTP as previously described²⁹. For pharmacological experiments, drugs (SBI, 0.5 μ M, Selleck; tBP, 0.1, 1 and 5 μ M, Selleck; TAT–GluA2_{3Y} peptide, 10 μ M, MCE; a designed tBP-scrambled (YGRKKRRQRRRG VGNDFFINHETTGFATEW), 1 μ M, MCE; TAT–GluA2_{3Y}-scrambled, 10 μ M, MCE; dyngo-4a, 5 μ M, MCE) were bath applied after 10 min of stable baseline recordings.

To measure the dosage effect of tBP (0.5, 1 and 5 μ M) in Lhb neurons from CRS mice, we designed an incubation experiment, in which tBP was bath perfused into the recording chamber and incubated for at least 10 min before recordings. The before and after effects of tBP on the same neuron were also measured to test the onset time of the drug effect.

Offline analysis of electrophysiological data was performed with Clampfit v.10.6 (Molecular Devices) and Mini Analysis Program (Synaptosoft).

The percentage of burst- and tonic-type spikes were obtained by the ratio of normalized tonic/bursting spike number to the total normalized spike number:

$$\begin{aligned} & \text{(Normalized tonic/bursting spike number)} \\ & = \text{Mean frequency of tonic/bursting neurons} \\ & \quad \times \text{percentage of tonic/bursting neurons;} \end{aligned}$$

$$\begin{aligned} & \text{Normalized total spike number} = \text{Mean frequency of tonic neurons} \\ & \quad \times \text{percentage of tonic neurons} + \text{Mean frequency of bursting neurons} \\ & \quad \times \text{percentage of bursting neurons} \end{aligned}$$

Statistical analysis and reproducibility

The required sample sizes were determined on the basis of our previous experience conducting similar experiments. For all experiments, mice were randomly grouped and investigators were blinded to group allocation during experimentation and data analysis. The offline data analysis was performed blindly with GraphPad Prism software v.8. Data points were excluded from analyses if the viral injection site or drug delivery site was out of the interested region. For all data, we first checked the normality and homogeneity of variance. The following statistical tests were used when applicable: two-sided paired or unpaired *t*-test, or two-sided unpaired *t*-test with Welch's correction, one-way analysis of variance (ANOVA) with Dunnett's multiple comparisons test, uncorrected Fisher's LSD test or Tukey's multiple comparisons test, Pearson correlation test and two-way ANOVA. In the case of non-Gaussian distributed data, we used the two-sided Wilcoxon test, two-sided Mann–Whitney test, and the Kruskal–Wallis test with an uncorrected Dunn's test. To compare the firing patterns and percentage of spikes of Lhb neurons, we used the two-sided chi-square test and Fisher's exact test. Data details are shown in the Source data. Data are presented as mean \pm s.e.m. All statistical tests were two-sided and statistical significance was set to $P < 0.05$.

For Fig. 5i and Extended Data Fig. 11c, immunofluorescence data are representative of three independent experiments. All experiments were conducted using at least two cohorts of animals. The results were reproducible across cohorts and combined for the final analysis.

Reporting summary

Further information on research design is available in the Nature Portfolio Reporting Summary linked to this article.

Data availability

All raw and processed sequencing data generated in this study have been deposited in the NCBI Gene Expression Omnibus under accession numbers GSE287175 (bulk RNA-seq) and GSE287308 (snRNA-seq). Raw, uncropped images of western blots are provided in the Supplementary Information. Source data are provided with this paper.

Code availability

There are no newly generated codes used in this paper.

50. Komatsu, M. et al. Impairment of starvation-induced and constitutive autophagy in *Atg7*-deficient mice. *J. Cell Biol.* **169**, 425–434 (2005).

Acknowledgements We thank E. N. Cahill, P. Shi, C. R. Ren, X. M. Li, B. M. Li, Y. Wang, G. Bai, Q. G. Zhou, F. Yang and N. Y. Lee for comments on the manuscript. This work was supported by grants from the STI2030 - Major projects (grant nos. 2022ZD0211700 to Y.C. and Z. Zhang); the National Natural Science Foundation of China (grant nos. 32371057, 32071017 and 31922031 to Y.C.; 32400830 to Y.D.); Non-profit Central Research Institute Fund of Chinese Academy of Medical Science (grant no. 2023-PT310-01 to Y.C.); the Fundamental Research Funds for the Central Universities (grant no. 226-2022-00149 to Y.C.); the Natural Science Foundation of Zhejiang Province (grant no. LDQ24C090001 to Y.C.); the CAS Youth Interdisciplinary Team (grant no. JCTD-2022-11 to Y.C.); Jinhua Science and Technology Plan Projects (grant no. 2023-3-170) to Xiangnan Zhang; the China Postdoctoral Science Foundation (grant nos. BX20230319 and 2024M752770 to Y.D.). We are grateful to W. Yin from the Core Facilities, Zhejiang University School of Medicine, Y. C. Zhang from the Center of Cryo-Electron Microscopy (CEEM), Zhejiang University for the technical assistance and M. Komatsu of Tokyo Metropolitan Institute of Medical Science for kindly offering the *Atg7^{flax/flax}* mice.

Author contributions Y.C. conceived, designed and supervised the study and interpreted the results with the help of Xiangnan Zhang and Y.D. Y.D., Xiangnan Zhang, Z. Zhang, Xuliang Zhang, H.M., Z.C. and W.Y. provided technical support and gave advice on experimental design. Xiangnan Zhang provided the transgenic mice. L.Y. performed transcriptome analysis,

western blot, electron microscopy, real-time qPCR and histology with the assistance of M.L., Y. Lu, Q.X., X.G., Y. Liu and Y.F. L.Y. and Z. Zheng performed behavioural assays and surgeries with the assistance of M.L., Q.X., Z.L., R.D. and R.M. C.G. performed electrophysiology recordings. L.Y., Z. Zheng and Y.D. performed fibre photometry. L.Y., C.G., Z. Zheng and Y.D. performed data analysis. L.Y., Z. Zheng and C.G. drafted the figures with the assistance of Y.D. Y.C. and Y.D. wrote the manuscript with the assistance of Z.D.

Competing interests The authors declare no competing interests.

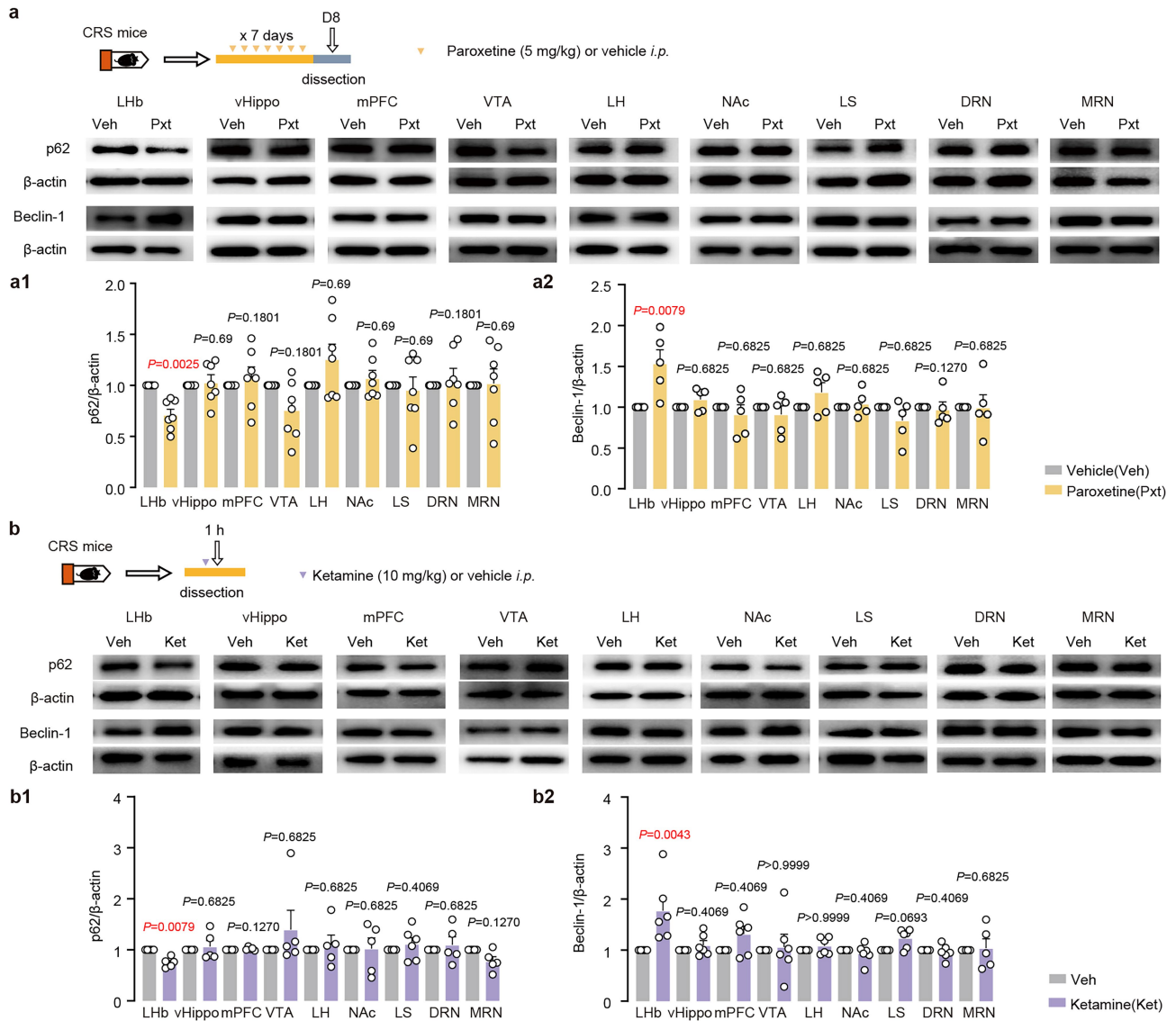
Additional information

Supplementary information The online version contains supplementary material available at <https://doi.org/10.1038/s41586-025-08807-4>.

Correspondence and requests for materials should be addressed to Xiangnan Zhang or Yihui Cui.

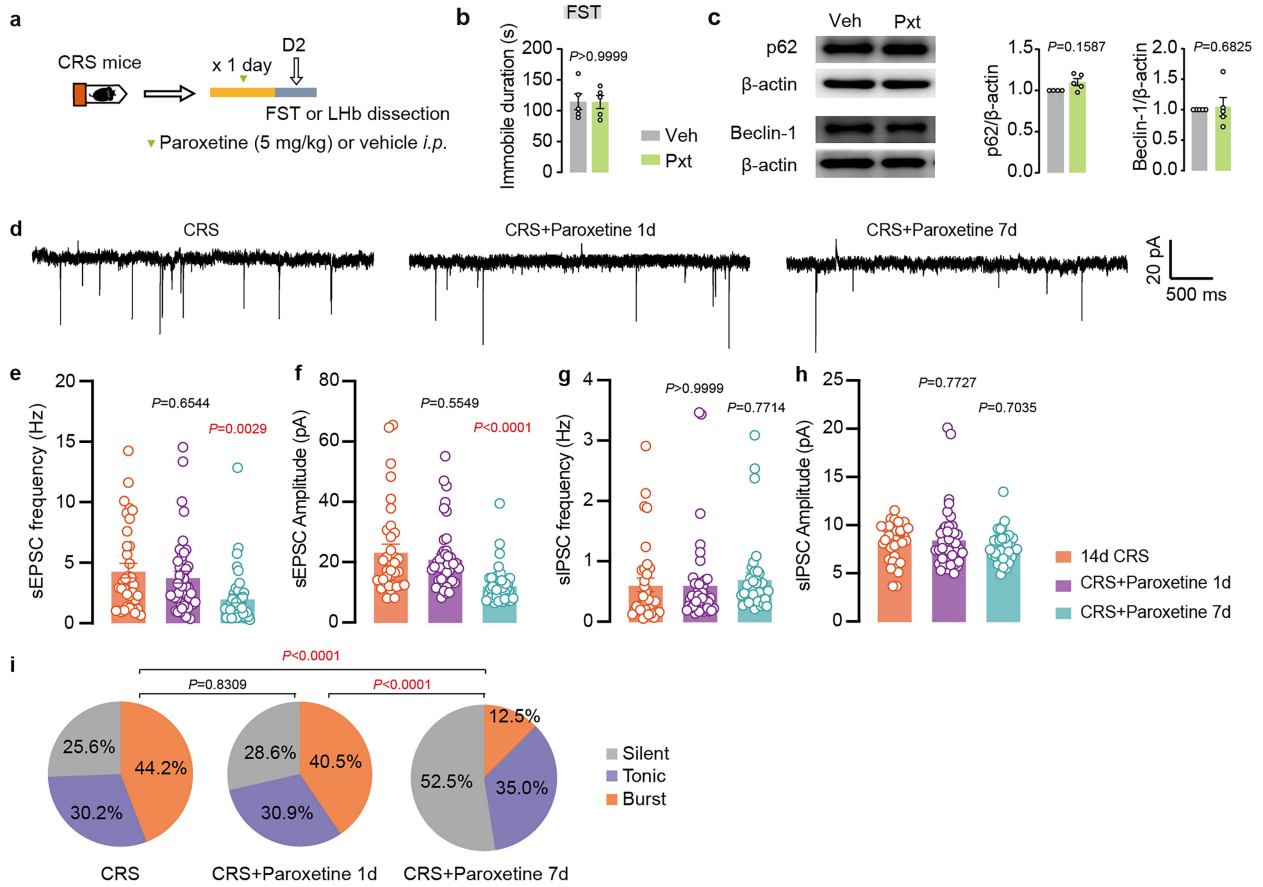
Peer review information *Nature* thanks Kaoru Inokuchi, Paul Kenny and the other, anonymous, reviewer(s) for their contribution to the peer review of this work. Peer reviewer reports are available.

Reprints and permissions information is available at <http://www.nature.com/reprints>.



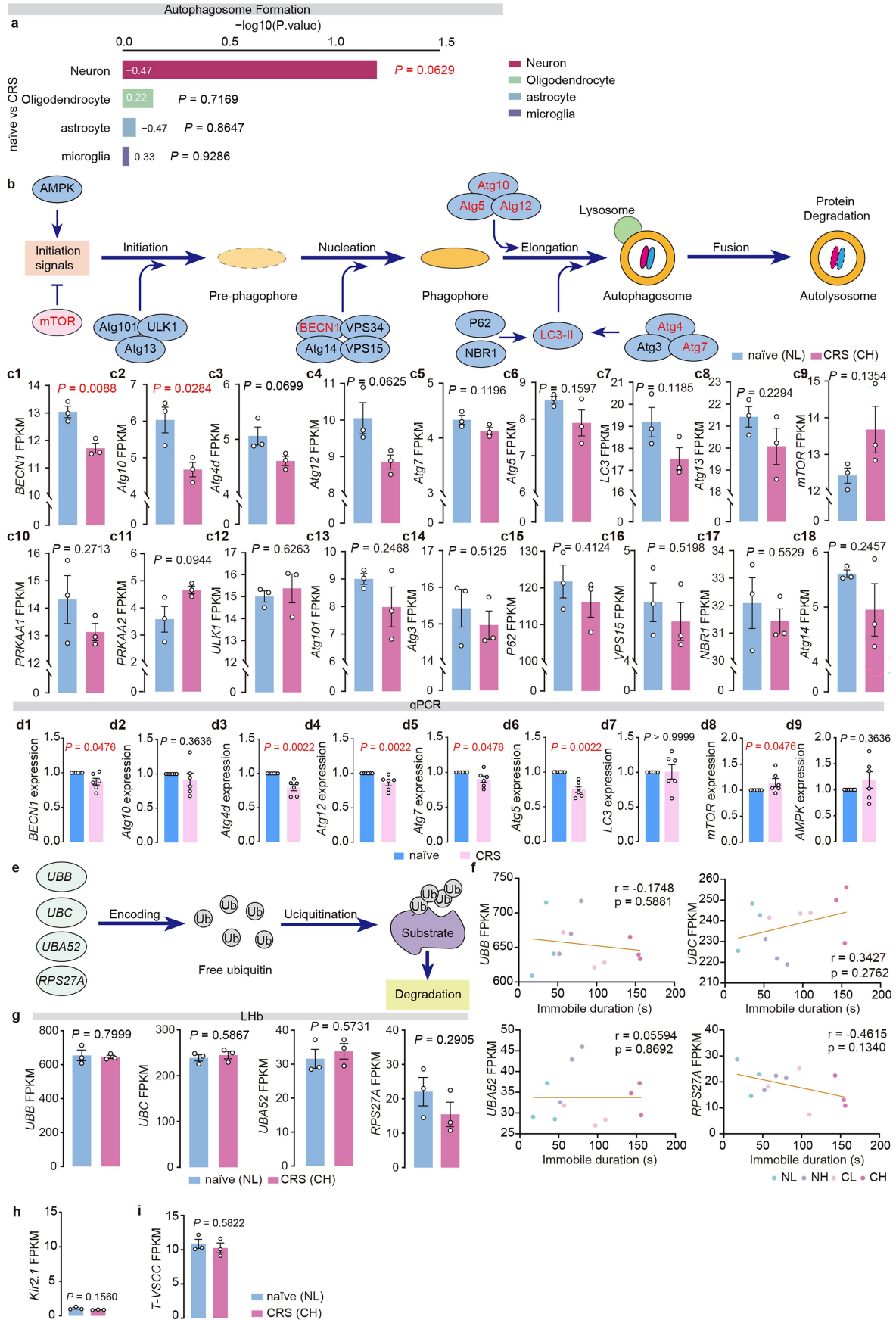
Extended Data Fig. 1 | Region-specific effect of chronic stress or antidepressants on brain autophagy. a, b, Antidepressant dose regimen of paroxetine (**a1**, LHb, $n_{\text{Veh/Pxt}} = 5/7$; $n_{\text{Veh/Pxt}} = 7$ for the rest of brain regions; **a2**, $n_{\text{Veh/Pxt}} = 5/\text{group}$) and ketamine (**b1**, $n_{\text{Veh/Pxt}} = 5/6$, for LS, $n_{\text{Veh/Pxt}} = 5$ for the rest of brain regions; **b2**, $n_{\text{Veh/Pxt}} = 5$ for MRN, $n_{\text{Veh/Pxt}} = 5/6$ for the rest of brain regions) treatment (*i.p.*) enhances autophagy (i.e., decreased p62 and increased Beclin-1) in LHb, but does not affect autophagy in vHippo, mPFC, VTA, LH, NAc,

LS, DRN and MRN of CRS mice. Two-sided Mann-Whitney test (**a1**, **a2**, **b1** and **b2**). Data are mean \pm s.e.m. LHb, lateral habenula; vHippo, ventral hippocampus; VTA, ventral tegmental area; NAc, nucleus accumbens; mPFC, medial prefrontal cortex; LH, lateral hypothalamus; LS, lateral septum; DRN, dorsal raphe; MRN, median raphe; Veh, vehicle; Pxt, paroxetine; Ket, ketamine; CRS, chronic restraint stress. Schematics in **a, b** adapted from ref. 31, Elsevier.



Extended Data Fig. 2 | Chronic but not acute administration of paroxetine enhances Lhb autophagy, normalizes Lhb neuronal hyperactivity and affects behavioral outcomes. a-c, Acute paroxetine treatment (*i.p.*) does not exert antidepressant-like effects (**b**, $n_{\text{Veh/Pxt}} = 5/\text{group}$) or alter Lhb autophagy (**c**, $n_{\text{Veh/Pxt}} = 4/5$ for p62, $n_{\text{Veh/Pxt}} = 5/\text{group}$ for Beclin-1) in CRS mice. **d-h,** Representative traces (**d**) and quantification (**e-h**) of synaptic activity under 1-day or 7-day *i.p.* injection of paroxetine in CRS mice (**e** and **f**, $N_{\text{CRS/CRS+paro1d/CRS+paro7d}} = 35/42/40$ neurons, $N_{\text{CRS/CRS+paro1d/CRS+paro7d}} = 4/5/5$ mice);

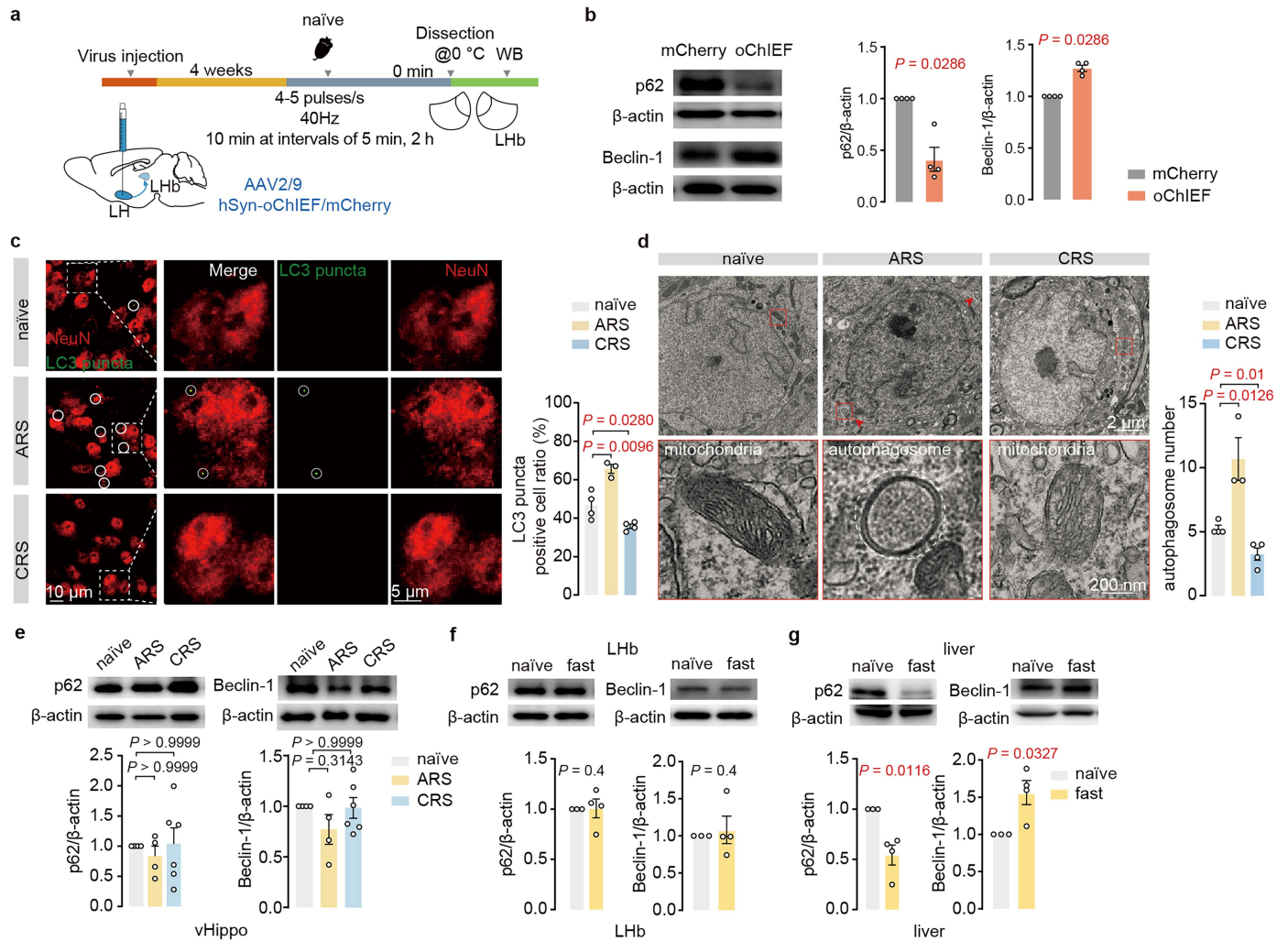
g and **h**, $N_{\text{CRS/CRS+paro1d/CRS+paro7d}} = 35/42/37$ neurons, $N_{\text{CRS/CRS+paro1d/CRS+paro7d}} = 4/5/5$ mice). **i,** Pie charts illustrating spontaneous firing activity of Lhb neurons under 1-day or 7-day *i.p.* injection of paroxetine in CRS mice ($N_{\text{CRS/CRS+paro1d/CRS+paro7d}} = 43/42/40$ neurons, $N_{\text{CRS/CRS+paro1d/CRS+paro7d}} = 5/5/5$ mice). Two-sided Mann-Whitney test (**b** and **c**), One way-ANOVA with Dunnett's multiple comparisons test (**e-h**), two-sided Chi-square (**i**). Data are mean \pm s.e.m. Schematic in **a** adapted from ref. 31, Elsevier.



Extended Data Fig. 3 | See next page for caption.

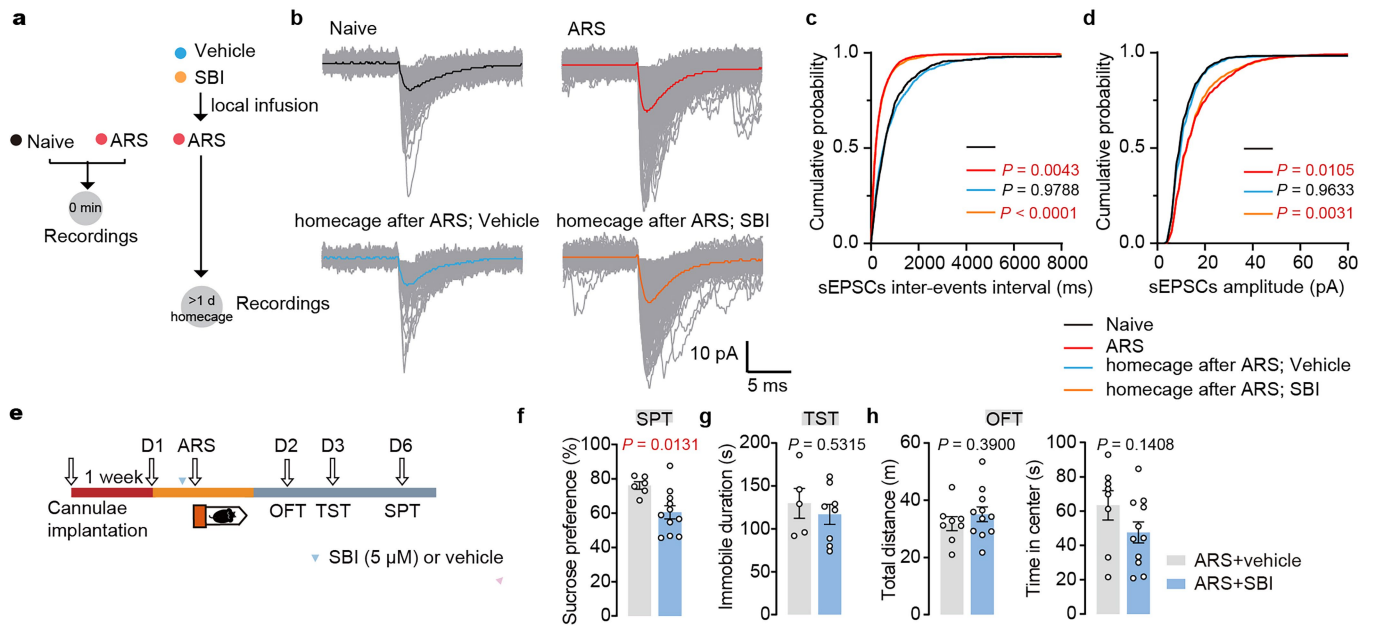
Extended Data Fig. 3 | Transcriptome data indicates attenuated autophagy function in LHb neurons. **a**, Single-nucleus sequencing showing neuronal and glial autophagosome formation pathway in naïve vs. CRS mice (n = 3 mice per group). **b**, Schematics of autophagy signaling. Genes annotated in red indicate the most altered genes listed in Panel c. **c1-c18**, Bar graphs showing autophagy-related mRNA expression level in LHb from naïve and CRS mice ($n_{\text{naïve/CRS}} = 3/\text{group}$). **d1-d9**, Quantification of qPCR experiments showing mRNA expression levels of autophagy-related genes after CRS. ($n_{\text{naïve/CRS}} = 6/\text{group}$).

e, Schematics of ubiquitin signaling. **f**, Correlation of *UBB*, *UBC*, *UBA52* and *RPS27A* mRNA FPKM with behavioral scores (immobile durations in FST) (n = 12 mice). **g**, Bar graphs showing ubiquitin-related mRNA expression level in LHb from CRS and naïve mice ($n_{\text{naïve/CRS}} = 3/\text{group}$). **h, i**, Quantification of mRNA levels of *Kir2.1* (**h**) and *T-VSCC* (**i**) in the LHb of naïve and CRS mice ($n_{\text{naïve/CRS}} = 3/\text{group}$). Two-sided Gene set variation analysis (**a**), two-sided Unpaired *t*-test (**c1-c18, g-i**), Two-sided Mann-Whitney test (**d1-d9**), Pearson correlation test (**f**). Data are mean \pm s.e.m.



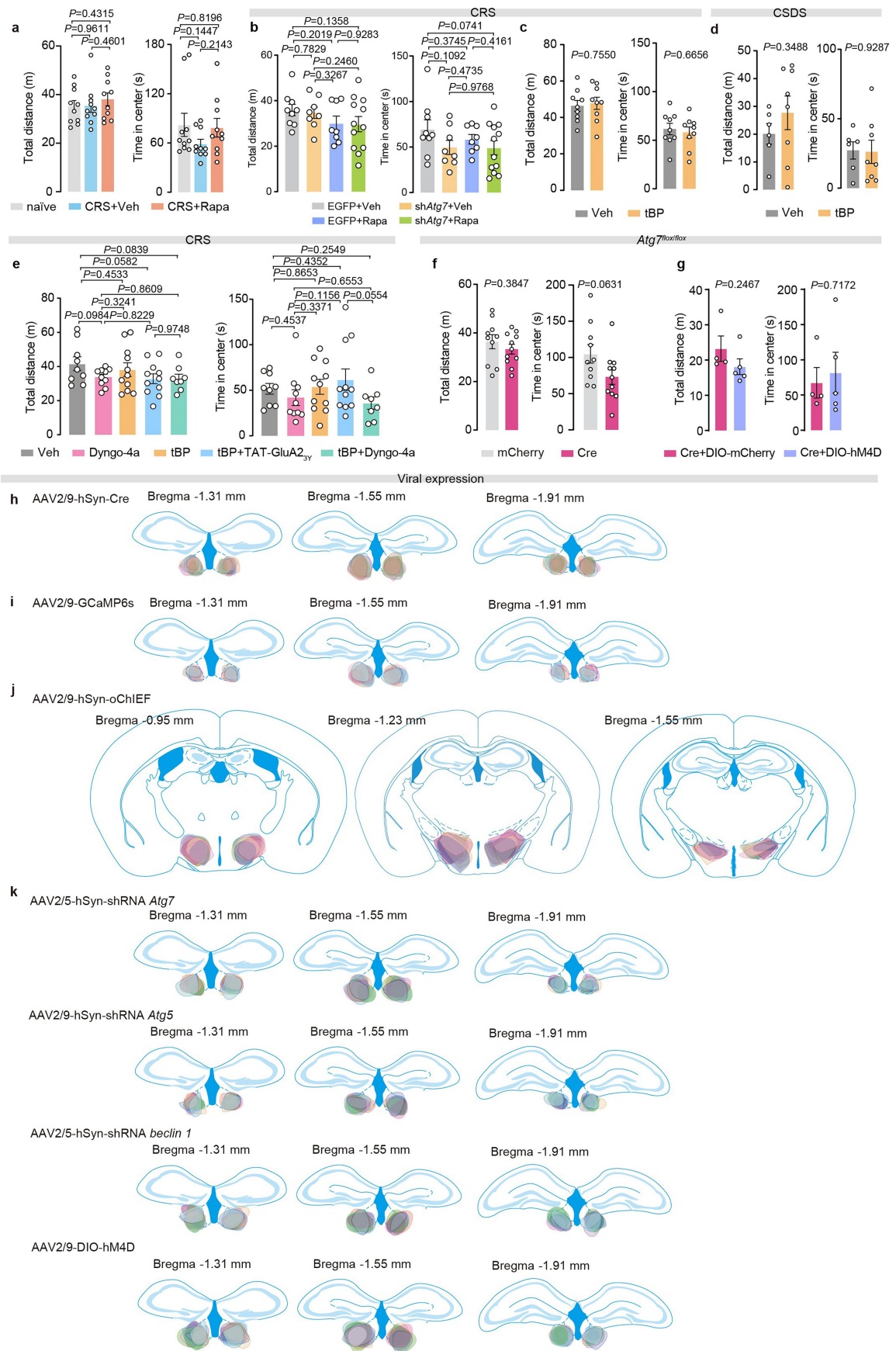
Extended Data Fig. 4 | Autophagy levels in the brain or peripheral organ under stress or fasting conditions. **a**, Experimental design. **b**, Representative images (left) and quantification (right) of western blot analysis showing 40-Hz phasic photostimulation at LH-LHb axonal terminals instantly decreased p62 and increased Beclin-1 levels ($n_{\text{mCherry/oChIEF}} = 4/\text{group}$). **c**, Representative images (left) and quantification (right) of proportion of LC3 puncta positive neurons in LHb of mice treated with ARS or CRS. White circles indicate the localization of LC3 puncta signals ($n_{\text{naïve/ARS/CRS}} = 4/3/4$). **d**, Representative images (left) and quantification (right) of electron microscopy showing the number of autophagosomes (quantified from 15 randomly selected neurons) in LHb of

mice treated with ARS or CRS. Red arrowheads indicate the location of autophagosomes. Dash lines circle the contour of a representative organelle ($n_{\text{naïve/ARS/CRS}} = 4/3/4$). **e**, Representative images (top) and quantification (bottom) of p62 or Beclin-1 western blot of vHippo samples from naïve, ARS or CRS mice ($n_{\text{naïve/ARS/CRS}} = 4/4/6$ for both p62 and Beclin-1). **f, g**, Representative images (top) and quantification (bottom) of p62 or Beclin-1 western blot of LHb (**f**) or liver (**g**) samples from naïve or 24h-fasted mice (**f** and **g**, $n_{\text{naïve/fast}} = 4/3/4$). Two-sided Unpaired *t*-test (**c**, **d**, and **g**), Two-sided Mann-Whitney test (**b**, **e** and **f**). Data are mean \pm s.e.m. Schematic in **a** adapted from ref. 31, Elsevier.



Extended Data Fig. 5 | Local infusion of SBI in LHb facilitates stress susceptibility and prevents the LTD-like process naturally occurring after acute stress. **a**, Experimental design. **b-d**, Representative traces (**b**) and quantification (**c,d**) of spontaneous excitatory neurotransmission immediately after ARS, or pre-treated with SBI or vehicle (Veh) and 1-3 days after ARS in the homecage (HC) (**c** and **d**, $n_{\text{naive/ARS/ARS+HC/Veh/ARS+HC+SBI}} = 39/32/43/37$ neurons,

6/5/5/5 mice). **e**, Experimental design. **f-h**, Local infusion of SBI in LHb before stress facilitates depression-like phenotype in mice (**f**, $n_{\text{ARS+Veh/ARS+SBI}} = 6/11$; **g**, $n_{\text{ARS+Veh/ARS+SBI}} = 5/8$; **h**, $n_{\text{ARS+Veh/ARS+SBI}} = 8/11$). One way-ANOVA with Uncorrected Fisher's LSD (**c**) or Dunnett's multiple comparisons test (**d**), two-sided Unpaired *t*-test (**f-h**). Data are mean \pm s.e.m. Schematic in **e** adapted from ref. 31, Elsevier.

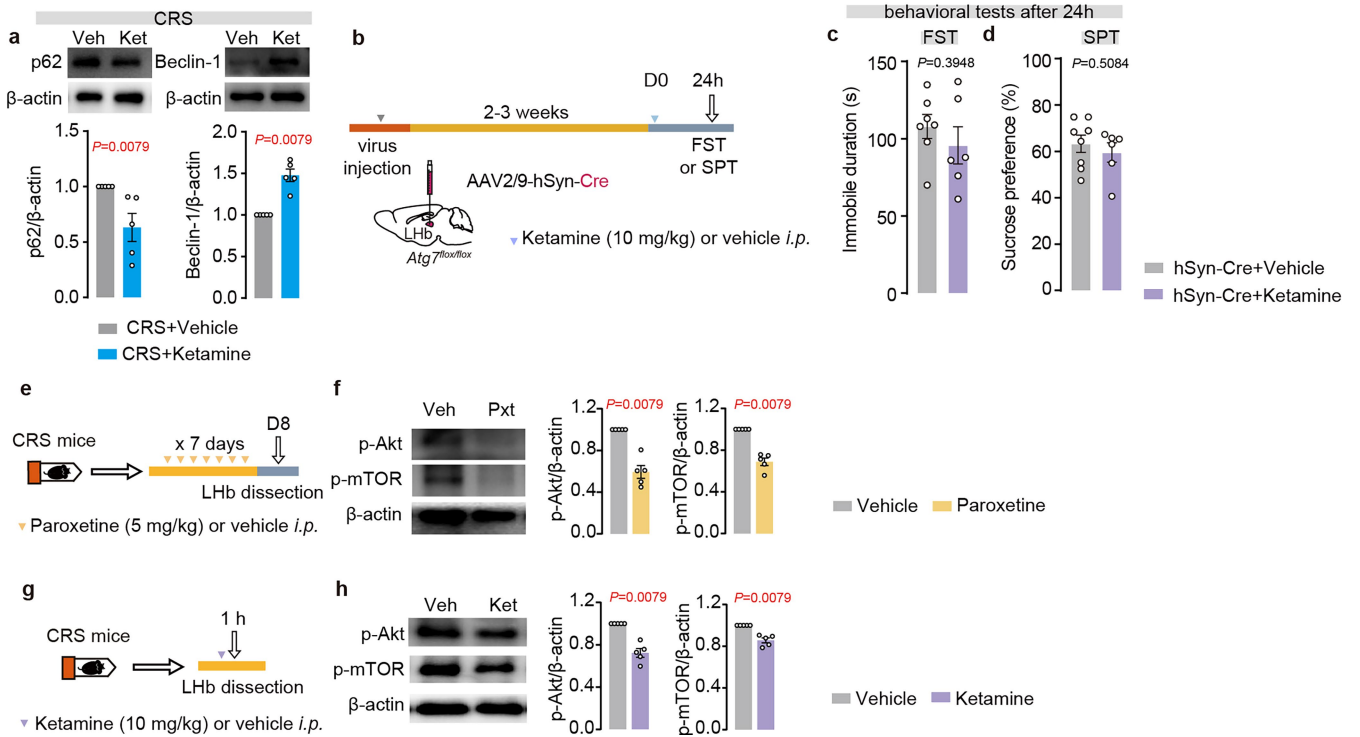


Extended Data Fig. 6 | See next page for caption.

Extended Data Fig. 6 | Behavioral performances in the OFT and viral expression profiles under different circumstances.

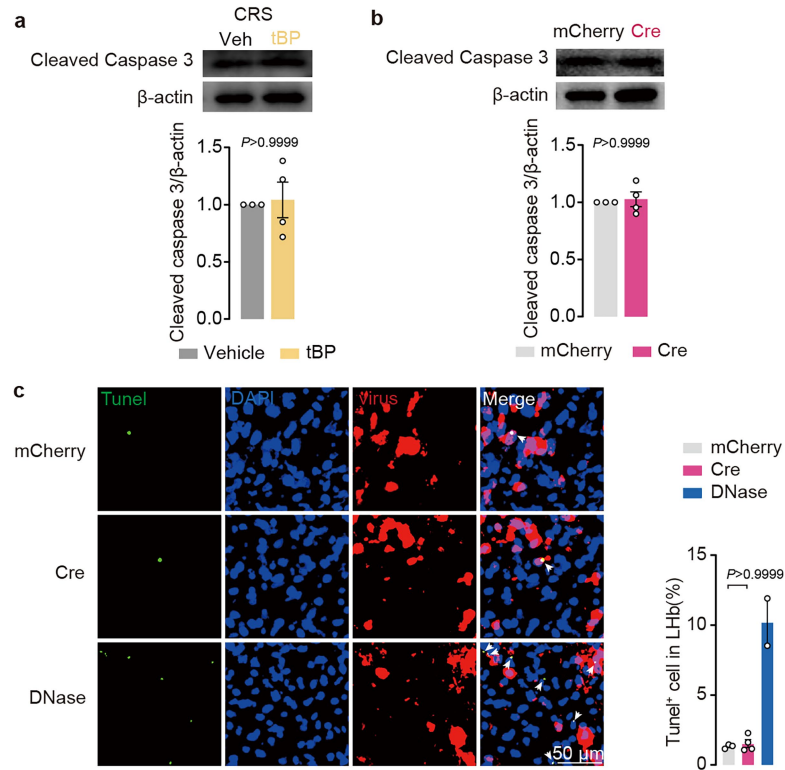
a, $n_{\text{naive/CRS+Veh/CRS+Rapa}} = 10/\text{group}$ for both OFT total distance and center time;
b, $n_{\text{EGFP+Veh/EGFP+Rapa/Atg7+Rapa/Atg7+Veh}} = 9/8/8/12$ for both OFT total distance and center time; **c**, $n_{\text{CRS/tBP}} = 9/\text{group}$ for both OFT total distance and center time; **d**, $n_{\text{CRS/tBP}} = 6/8$ for both OFT total distance and center time;

e, $n_{\text{Veh/dyngo/tBP/tBP+TAT-GluA23y/dyngo+tBP}} = 9/10/11/11/8$ for both OFT total distance and center time; **f**, $n_{\text{mCherry/Cre}} = 10/11$ for both OFT total distance and center time; **g**, $n_{\text{dio-mCherry/dio-hM4D}} = 4/5$ for both OFT total distance and center time. **h-k**, viral expression profiles under different circumstances. One way-ANOVA with Uncorrected Fisher's LSD (**a**, **b** and **e**), two-sided Unpaired *t*-test (**c** and **d**, **f** and **g**). Data are mean \pm s.e.m. Schematics in **h-k** adapted from ref. 31, Elsevier.



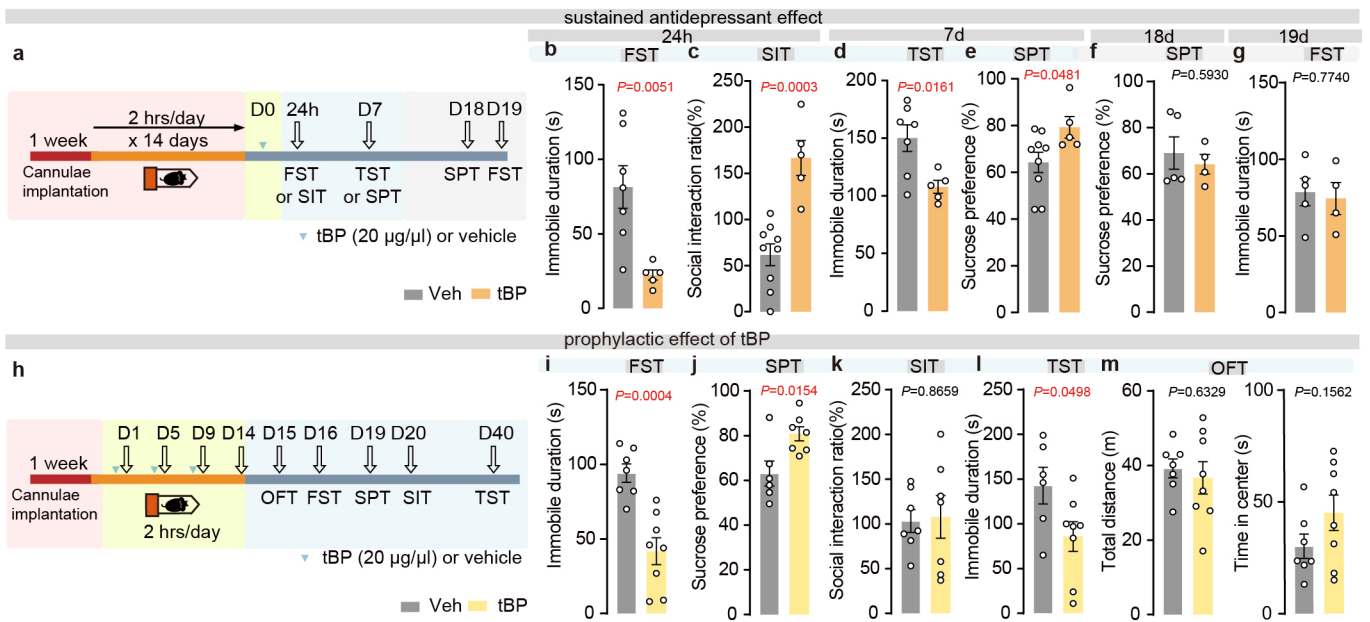
Extended Data Fig. 7 | Lhb autophagy plays essential roles in antidepressant-like effects of both paroxetine and ketamine. **a**, Antidepressant dosage of ketamine enhances autophagy (i.e., decreased p62 and increased Beclin-1) in Lhb 24 h after *i.p.* injection ($n_{\text{CRS+Veh/CRS+Ket}} = 5/\text{group}$). **b**, Experimental design. **c,d**, Ketamine does not affect FST and SPT scores in $Atg7^{\text{Lhb-/-}}$ mice (**c**, $n_{\text{Cre+Veh/Cre+Ket}} = 7/6$; **d**, $n_{\text{Cre+Veh/Cre+Ket}} = 8/6$). **e**, Experimental design. **f**, Paroxetine

treatment (*i.p.*, 7 d) decreased p-Akt and p-mTOR levels in the Lhb ($n_{\text{Veh/Paro}} = 5/\text{group}$). **g**, Experimental design. **h**, Ketamine treatment (*i.p.*) decreased p-Akt and p-mTOR levels in the Lhb ($n_{\text{Veh/Paro}} = 5/\text{group}$). Two-sided Mann-Whitney test (**a**, **f** and **h**) and two-sided Unpaired *t*-test (**c** and **d**). Data are mean \pm s.e.m. Schematic in **b** adapted from ref. 29, Elsevier; schematics in **e,g** adapted from ref. 31, Elsevier.



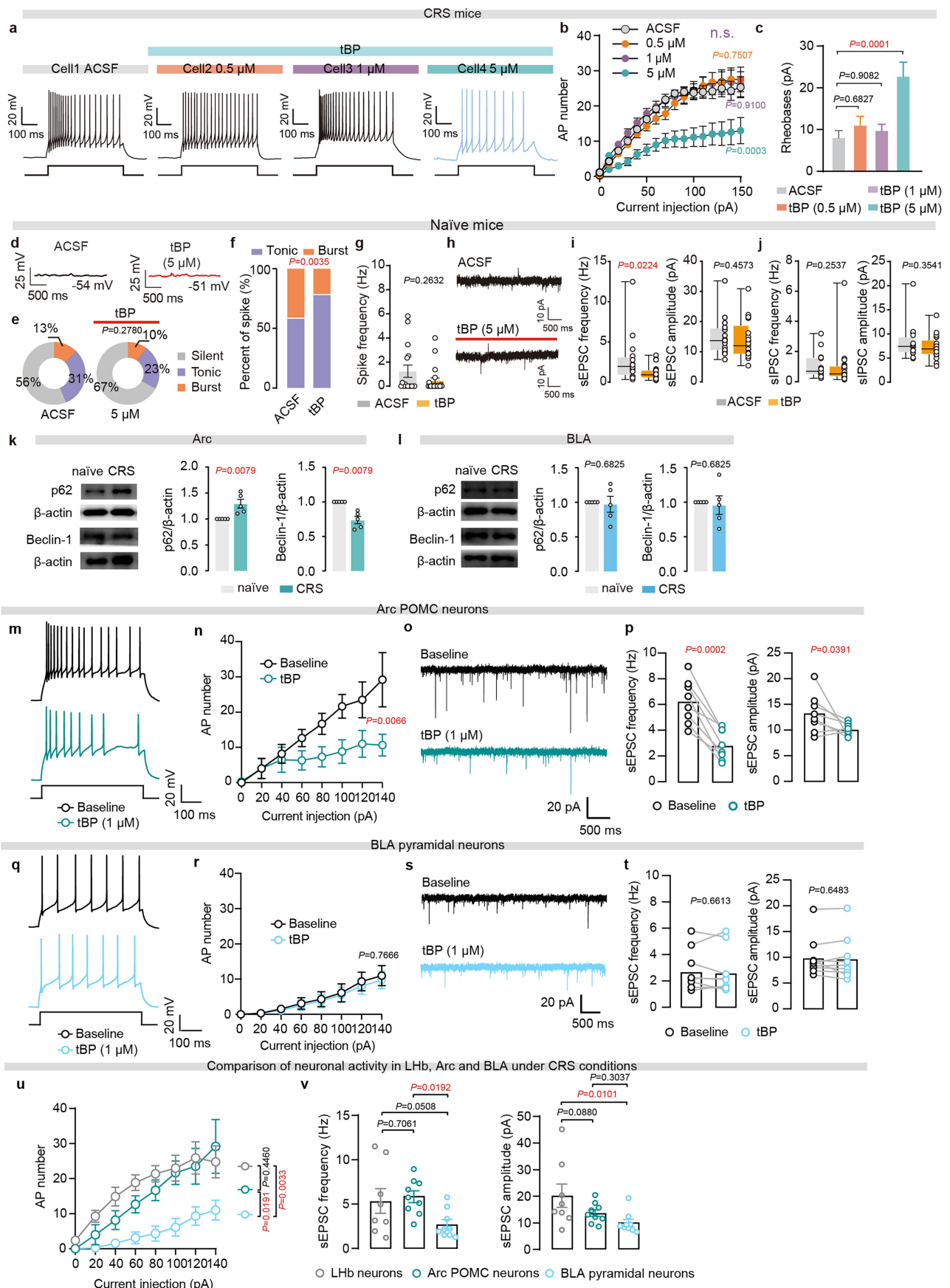
Extended Data Fig. 8 | Genetic ablation of *Atg7* in LHB or pharmacological enhancement of LHB autophagy does not induce neuronal apoptosis.
a,b, Western blot of cleaved caspase 3 shows that tBP treatment or knockout of *Atg7* does not induce apoptosis in LHB (**a**, $n_{\text{tBP/Veh}} = 3/4$; **b**, $n_{\text{mCherry/Cre}} = 3/4$). **c**, TUNEL

immunostaining shows that knock-out of *Atg7* in LHB does not induce neuronal apoptosis (**c**, $n_{\text{mCherry/Cre/DNase}} = 3/4/2$; DNase as a positive control). Two-sided Mann-Whitney test for all. Data are mean \pm s.e.m.



Extended Data Fig. 9 | Local infusion of tBP into the LHB exerts sustained and prophylactic antidepressant-like effects. a,h, Experimental designs. **b,c**, tBP decreases immobile duration in FST (**b**, $n_{\text{tBP/Veh}} = 7/5$) and increases social interaction ratio in SIT (**c**, $n_{\text{tBP/Veh}} = 9/5$) 24 h after tBP treatment. **d,e**, tBP decreases immobile duration in TST (**d**, $n_{\text{tBP/Veh}} = 7/5$) and increases sucrose preference (**e**, $n_{\text{tBP/Veh}} = 9/5$) in SPT 7 d after tBP treatment. **f,g**, tBP does not affect SPT (**f**, $n_{\text{tBP/Veh}} = 5/4$) and FST (**g**, $n_{\text{tBP/Veh}} = 5/4$) phenotypes 18–19 d after tBP

treatment. **i-m**, Prophylactic treatment of tBP decreases immobile duration in FST and TST (**i**, $n_{\text{tBP/Veh}} = 7/8$; **l**, $n_{\text{tBP/Veh}} = 6/8$), increases sucrose preference in SPT (**j**, $n_{\text{tBP/Veh}} = 6/7$), without affecting social interaction ratio (**k**, $n_{\text{tBP/Veh}} = 7/\text{group}$) and locomotion or anxiety-like behavior (**m**, $n_{\text{tBP/Veh}} = 7/8$). Two-sided Mann-Whitney test (**b**) and Two-sided Unpaired *t*-test (**c-g, i-m**). Data are mean \pm s.e.m. Schematics in **a,h** adapted from ref. 31, Elsevier.

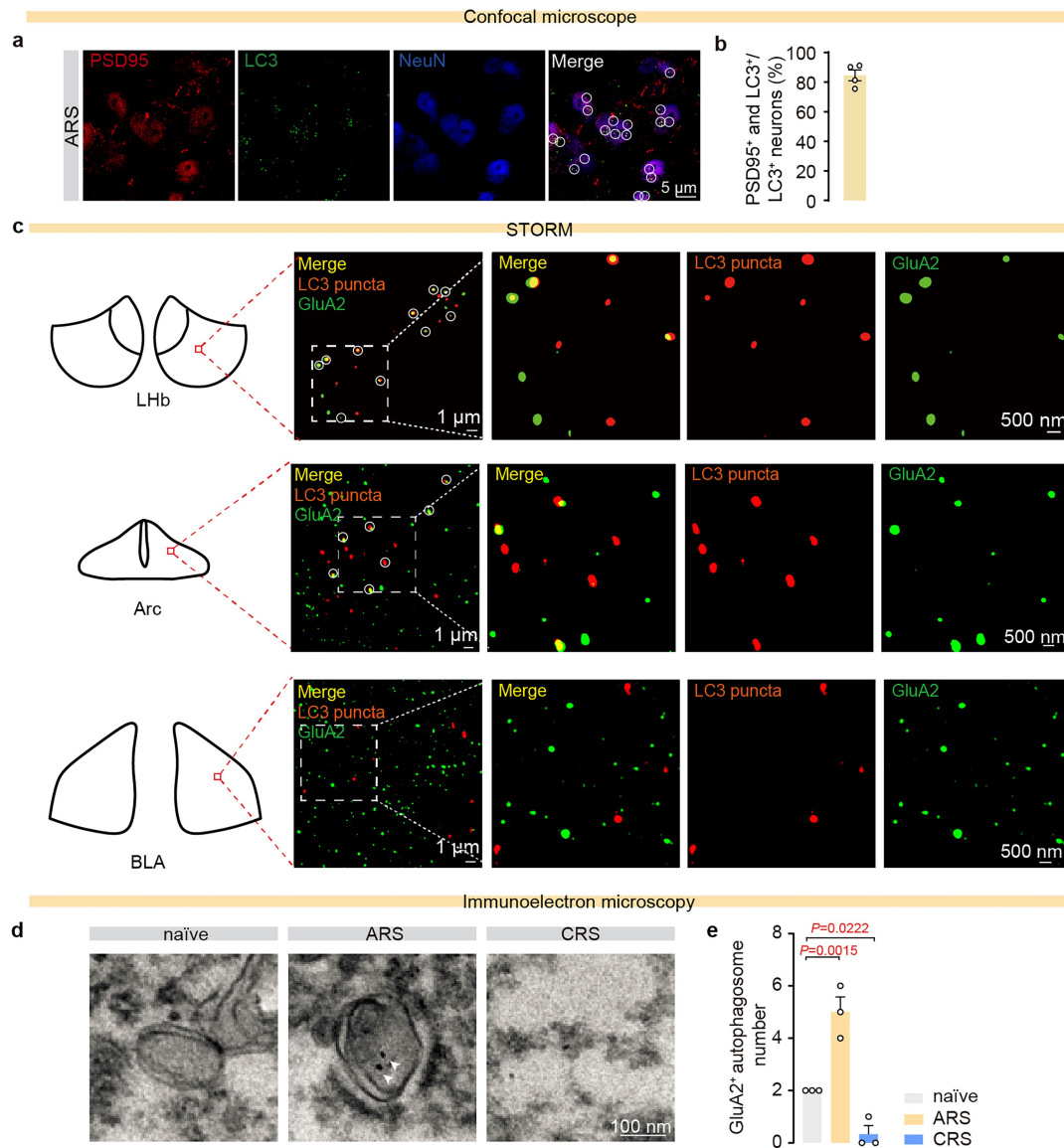


Extended Data Fig. 10 | See next page for caption.

Article

Extended Data Fig. 10 | Dose and activity-dependent effect of tBP on neuronal activity. **a-c**, Representative traces (**a**), quantification of neuronal excitability (**b**, $n_{ACSF/0.5/1/5} = 35/24/29/18$ neurons, $3/2/2/2$ mice) and rheobases (**c**, $n_{ACSF/0.5/1/5} = 30/31/37/23$ neurons, $3/2/2/2$ mice). **d-g**, Representative traces (**d**), pie charts (**e**) and bar graphs (**f,g**) showing the effects of tBP on spontaneous firing properties of LHB neurons in naïve mice (**e-g**, $n_{ACSF/5} = 16/21$ neurons, $2/2$ mice). **h-j**, Representative traces (**h**) and quantification (**i,j**) showing the effect of tBP incubation on spontaneous transmission in LHB neurons from naïve mice (**i and j**, $n_{ACSF/5} = 16/21$ neurons, $2/2$ mice). **k,l**, Representative images of Western Blot and quantification of p62 and Beclin-1 levels in the Arc (**k**) and BLA (**l**) after CRS (**k and l**, $n_{naïve/CRS} = 5/\text{group}$). **m,n**, Representative traces (**m**) and quantification (**n**, $n_{base/tBP} = 6$ neurons, 4 mice) of excitability in Arc POMC

neurons treated with tBP. **o,p**, Representative traces (**o**) and quantification (**p**, $n_{base/tBP} = 8$ neurons, 4 mice) of sEPSCs in Arc POMC neurons treated with tBP. **q,r**, Representative traces (**q**) and quantification (**r**, $n_{base/tBP} = 9$ neuron, 4 mice) of excitability in BLA PNs treated with tBP. **s,t**, Representative traces (**s**) and quantification (**t**, $n_{base/tBP} = 9$ neurons, 4 mice) of sEPSCs in BLA PNs treated with tBP. **u,v**, Comparison of excitability (**u**, $n_{Lhb/Arc/BLA} = 8/6/9$ neurons, $8/4/4$ mice) and sEPSCs (**v**, $n_{Lhb/Arc/BLA} = 8/9/9$ neurons, $8/4/4$ mice) in LHB neurons, Arc POMC neurons and BLA PNs. Two-sided Unpaired *t*-test (**b**, **n** and **r**), Two-sided Mann-Whitney test (**g**, **i-l**), Two-sided Paired *t*-test (**p** and **t**), Two-sided Wilcoxon test (**p**), One-way ANOVA with Dunnett's multiple comparisons test (**c**) or Uncorrected Fisher's LSD (**u** and **v**), two-sided Chi-square (**e**) and two-sided Fisher's exact test (**f**). Data are mean \pm s.e.m.

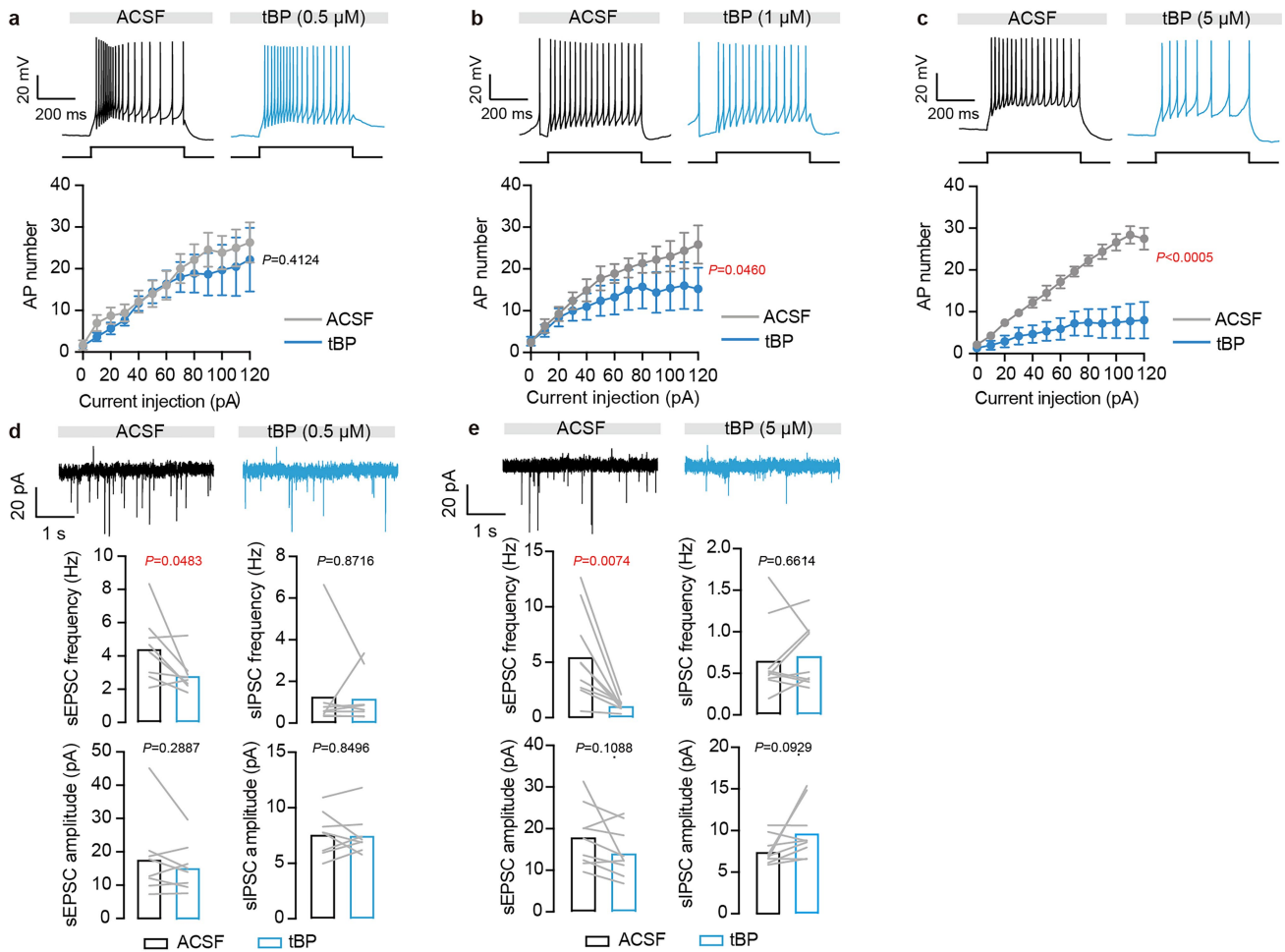


Extended Data Fig. 11 | Autophagosomes are mostly co-localized with a post-synaptic marker PSD95 and co-labeled with GluRs in LHB.

a,b, Representative images (**a**) and quantification (**b**) showing co-localization of PSD95 and LC3 in LHB neurons of mice treated with ARS ($n = 4$ mice).

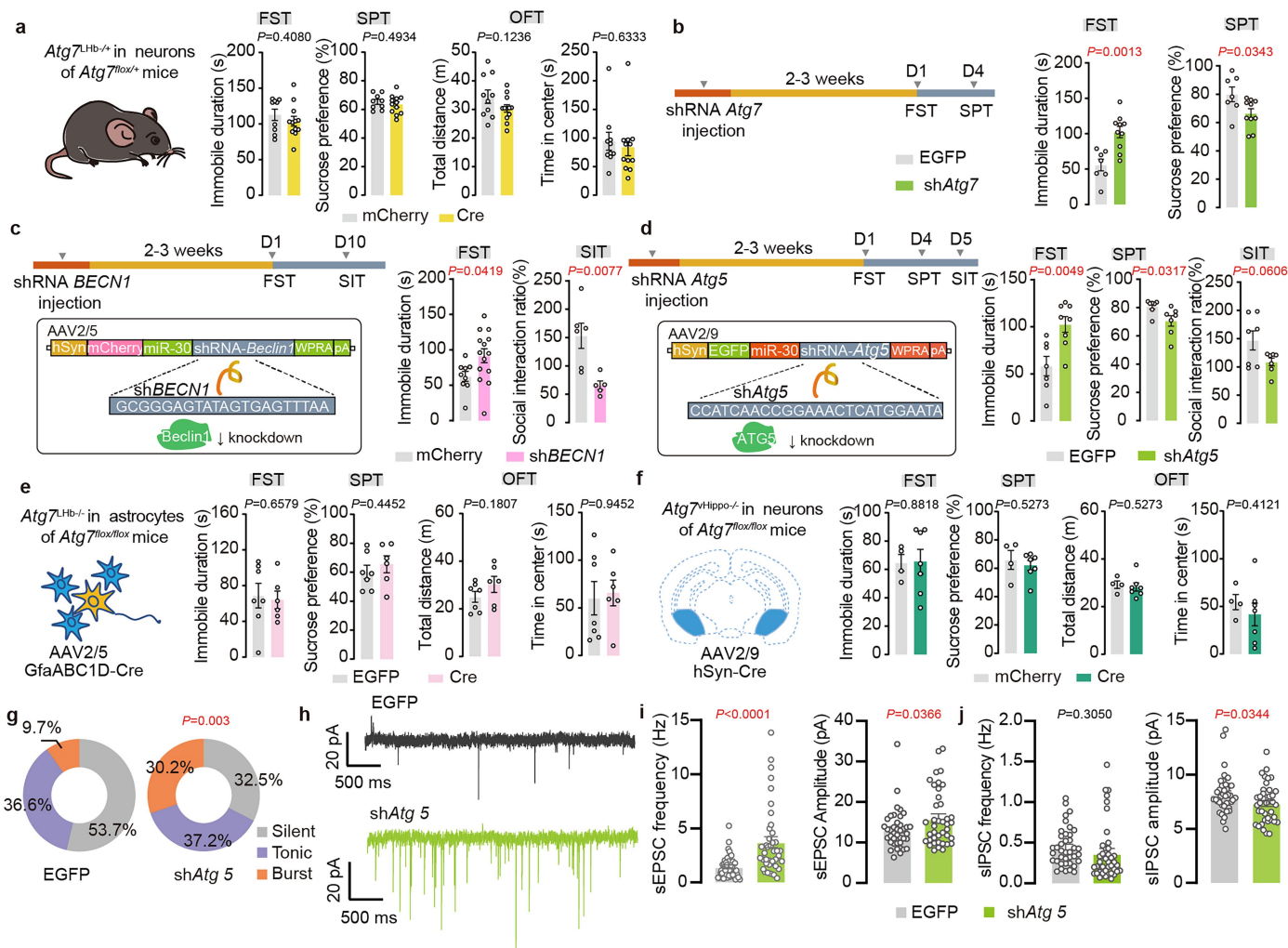
c, Representative STORM images showing localization of GluA2 (green) and LC3 puncta (red) in LHB, Arc and BLA from ARS-treated mice. **d,e**, Representative

immunoelectron microscopy images (**d**, $n_{\text{naive/ARS/CRS}} = 3/\text{group}$) and quantification (**e**) showing GluA2 immunoreactivity co-localized within autophagosomes (quantified from 15 randomly selected neurons) in LHB from mice treated with ARS or CRS. One-way ANOVA with Uncorrected Fisher's LSD (**e**). Data are mean \pm s.e.m.



Extended Data Fig. 12 | tBP rapidly decreases neuronal excitability and excitatory synaptic transmission. **a-c**, Representative traces (top) and quantification (bottom) showing neuronal excitability before and after tBP perfusion in Lhb neurons of CRS mice (**a**, $n_{\text{ACSF/tBP}} = 7/6$ neurons, 7 mice; **b**, $n_{\text{ACSF/tBP}} = 8/8$ neurons, 6 mice; **c**, $n_{\text{ACSF/tBP}} = 8/8$ neuron, 6 mice). **d,e**, Representative traces (top) and quantification (bottom) showing

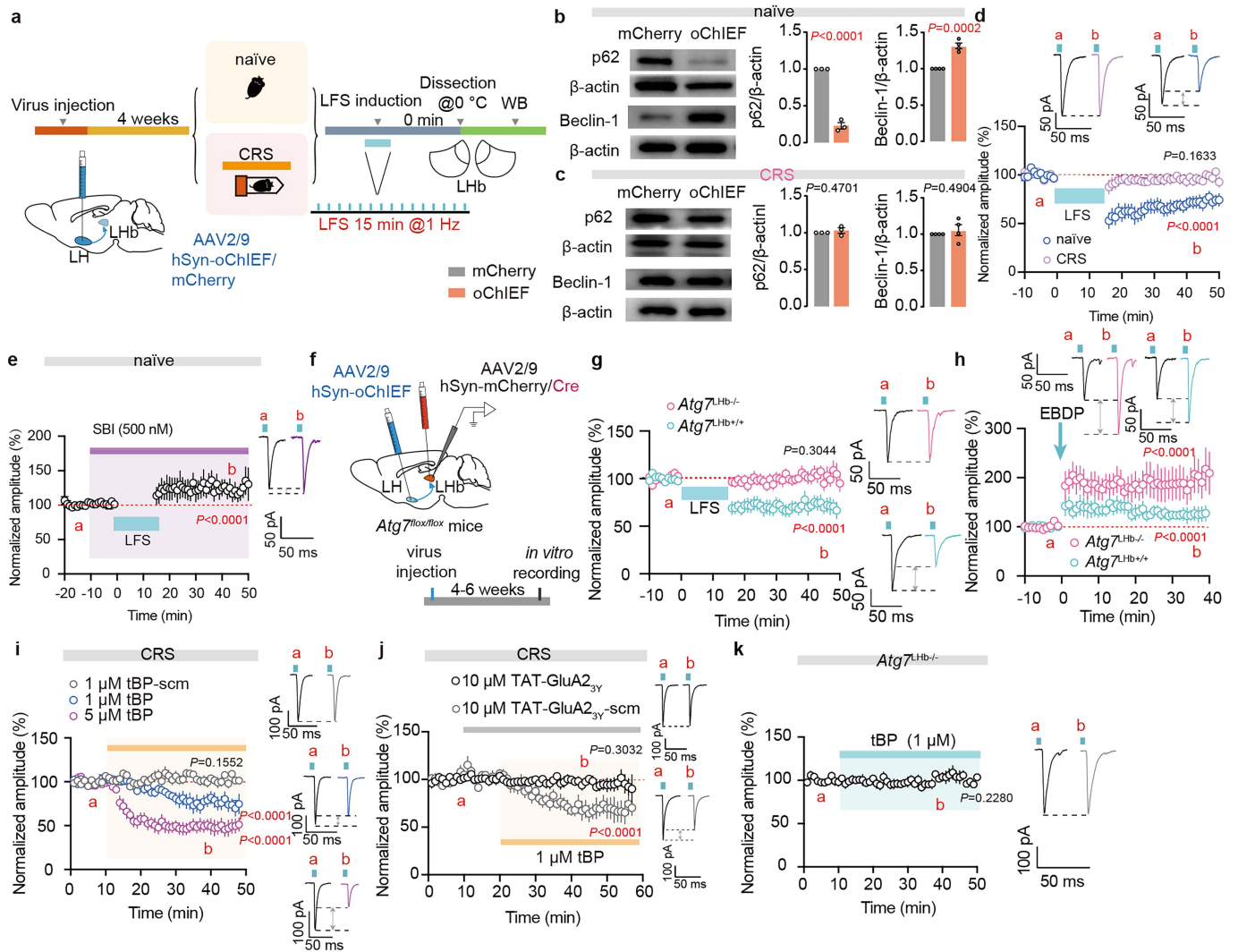
spontaneous neural transmission before and immediately after tBP perfusion in Lhb neurons of CRS mice (**d**, $n_{\text{ACSF/tBP}} = 8/8$ neurons, 7 mice for both sEPSCs and sIPSCs; **e**, $n_{\text{ACSF/tBP}} = 9/9$ neurons, 6 mice for both sEPSCs and sIPSCs). Two-sided Unpaired *t*-test (**a-c**) and Two-sided Paired *t*-test (**d** and **e**). Data are mean \pm s.e.m.



Extended Data Fig. 13 | Impairment of autophagy in LHB neurons directly drives depression-like behaviors and neuronal hyperfunctions.

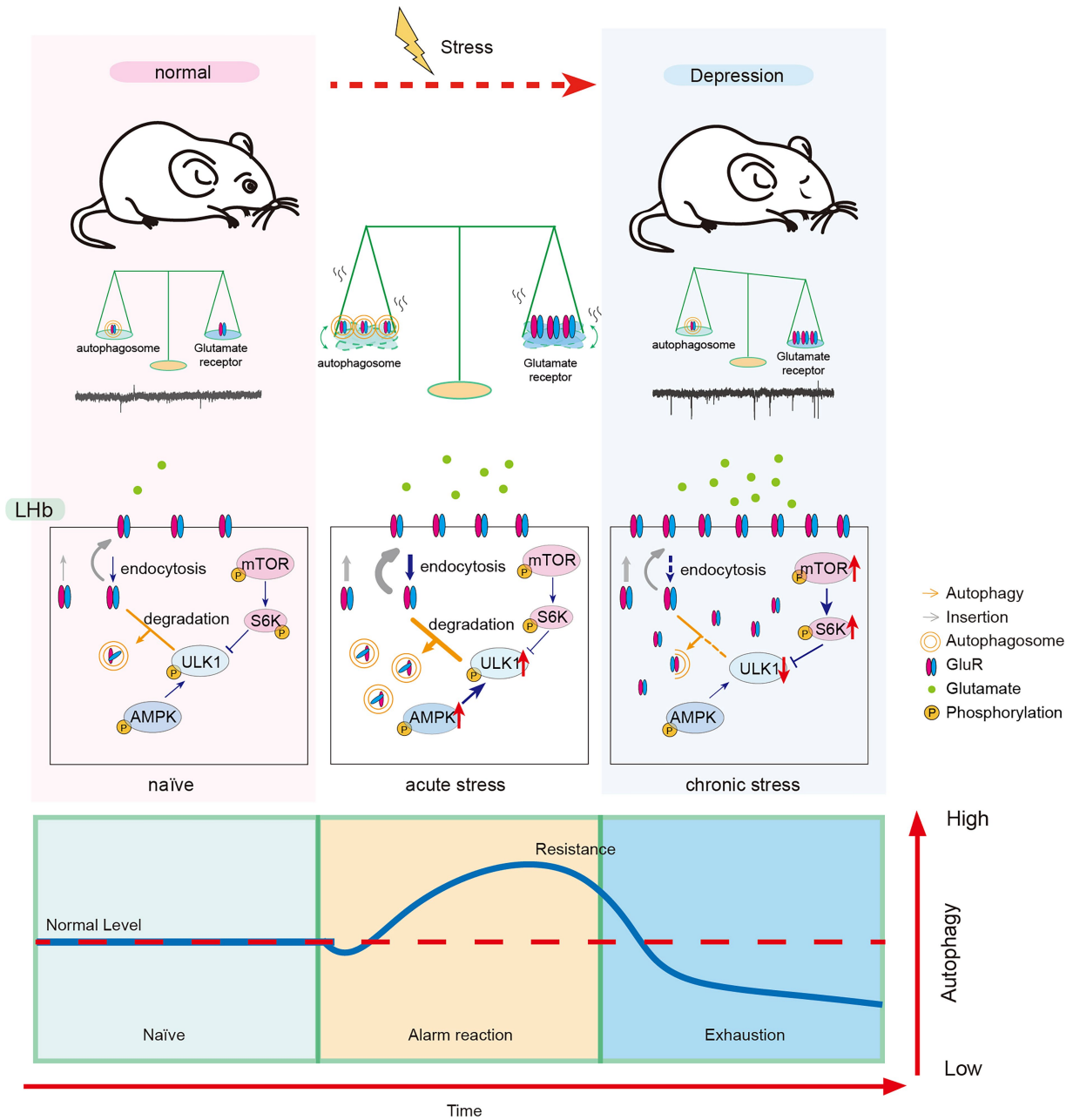
a, Conditional hemi knock-out of *Atg7* in LHB neurons of heterozygotes fails to induce depressive-like phenotypes ($n_{\text{mCherry}/\text{Cre}} = 9/12$ for FST and SPT; $n_{\text{mCherry}/\text{Cre}} = 10/12$ for OFT). **b**, Conditional knock down of *Atg7* with shRNA-*Atg7* directly leads to increased immobile duration in FST and decreased sucrose preference in SPT ($n_{\text{EGFP}/\text{shAtg7}} = 7/10$ for FST and SPT). **c**, Experimental designs and conditional knock-down of *BECN1* with shRNA-*BECN1* directly leads to increased immobile duration in FST and decreased social interaction ratio in SIT ($n_{\text{mCherry}/\text{shBECN1}} = 9/14$ for FST, $n_{\text{mCherry}/\text{shBECN1}} = 6/5$ for SIT). **d**, Conditional knock-down of *Atg5* with shRNA-*Atg5* directly leads to increased immobile duration in FST, decreased sucrose preference in SPT, and decreased trends of social interaction ratio in

SIT ($n_{\text{EGFP}/\text{shAtg5}} = 7/8$ for FST, $n_{\text{EGFP}/\text{shAtg5}} = 7/7$ group for SPT and SIT). **e**, Conditional knock-out of *Atg7* in LHB astrocytes fails to induce depressive-like phenotypes ($n_{\text{EGFP}/\text{Cre}} = 7/6$ for FST, SPT and SIT). **f**, Conditional knock-out of *Atg7* in vHippo neurons fails to induce depressive-like phenotypes ($n_{\text{mCherry}/\text{Cre}} = 4/7$ for FST, SPT and SIT). **g**, Pie charts illustrating the percentage of three types of LHB neurons with *Atg5* knock-down and its EGFP controls ($n_{\text{EGFP}/\text{shAtg5}} = 41/40$ neurons, $n_{\text{EGFP}/\text{shAtg5}} = 5/5$ mice). **h-j**, Representative traces (**h**) and quantification (**i-j**) of spontaneous neurotransmission in LHB neurons with *Atg5* deficiency (**i**, $n_{\text{EGFP}/\text{shAtg5}} = 40/40$ neurons, $n_{\text{EGFP}/\text{shAtg5}} = 5/5$ mice; **j**, $n_{\text{EGFP}/\text{shAtg5}} = 39/40$ neurons, $n_{\text{EGFP}/\text{shAtg5}} = 5/5$ mice). Two-sided Unpaired *t*-test (**a-d**, **i** and **j**), Two-sided Mann-Whitney test (**e** and **f**) and two-sided Chi-square (**g**). Data are mean \pm s.e.m.



Extended Data Fig. 14 | Autophagy controls the occurrence and magnitude of LHB synaptic plasticity. **a**, Experimental design. **b,c**, Representative images (left) and quantification (right) of p62 or Beclin-1 western blot showing LTD induction protocol instantly enhances autophagy level in LHb of naive mice (i.e., decreased p62 and increased Beclin-1 (**b**, $n_{\text{mCherry/oChIEF}} = 3/\text{group}$ for p62, $n_{\text{mCherry/oChIEF}} = 4/\text{group}$ for Beclin-1) but not CRS mice (**c**, $n_{\text{mCherry/oChIEF}} = 3/\text{group}$ for p62, $n_{\text{mCherry/oChIEF}} = 4/\text{group}$ for Beclin-1). **d**, LFS fails to induce LTD in the LHb of CRS mice ($n_{\text{naive}} = 9$ neurons, 7 mice; $n_{\text{CRS}} = 11$ neurons, 7 mice). **e**, SBI abolishes the LTD induction and induces a slight but significant LTP in LHb neurons ($n = 7$ neurons, 6 mice). **f**, Schematics of stereotaxic surgeries. **g**, Conditional knock-out of *Atg7* abolishes LTD in LHb neurons ($n_{\text{Atg7}^{+/+}} = 11$ neurons, 6 mice;

$n_{\text{Atg7}^{-/-}} = 10$ neurons, 7 mice). **h**, Kinetics and representative traces showing conditional knock-out of *Atg7* increases the LTP magnitude in LHb neurons ($n_{\text{Atg7}^{+/+}} = 8$ neurons, 3 mice; $n_{\text{Atg7}^{-/-}} = 10$ neurons, 8 mice). **i**, tBP, but not tBP-scm, directly induces dose-dependent pharmacological LTD in the LHb of CRS mice (1 μ M tBP, $n = 10$ neurons, 8 mice; 5 μ M tBP, $n = 11$ neurons, 7 mice; 1 μ M tBP-scm, $n = 10$ neurons, 7 mice). **j**, TAT-GluA2_{3Y} peptide, but not its scrambled analog (TAT-GluA2_{3Y}-scm), disrupts the tBP-induced LTD in the LHb of CRS mice (TAT-GluA2_{3Y}, $n = 9$ neurons, 6 mice; TAT-GluA2_{3Y}-scm, $n = 9$ neurons, 7 mice). **k**, tBP fails to induce LTD in the LHb of *Atg7^{LHb-/-}* mice ($n = 11$ neurons, 7 mice). Two-sided Unpaired *t*-test for all. Data are mean \pm s.e.m. Schematics in **a,f** adapted from ref. 29, Elsevier.



Extended Data Fig. 15 | Hypothesized model. Lhb autophagy is switched on rapidly in an energy-dependent manner (within minutes) via AMPK phosphorylation, acting as the “alarm reaction” phase of stress. As stress exposure persists, excitatory afferents onto Lhb are gradually potentiated, and Lhb autophagy may be constantly recruited for degrading excessive synaptic GluRs, resulting in the “resistance” phase. During the late phase of

chronic stress, Lhb autophagy is suppressed by the over-activation of mTOR signaling. Consequently, Lhb autophagy is incapable of counterbalancing the excessive synaptic weight through GluRs degradation, therefore slowing down towards GluRs endocytosis and causing the “exhaustion” phase of stress, neuronal hyperactivity and depression-like phenotypes. Adapted from ref. 29, Elsevier.

Reporting Summary

Nature Portfolio wishes to improve the reproducibility of the work that we publish. This form provides structure for consistency and transparency in reporting. For further information on Nature Portfolio policies, see our [Editorial Policies](#) and the [Editorial Policy Checklist](#).

Statistics

For all statistical analyses, confirm that the following items are present in the figure legend, table legend, main text, or Methods section.

n/a Confirmed

- The exact sample size (n) for each experimental group/condition, given as a discrete number and unit of measurement
- A statement on whether measurements were taken from distinct samples or whether the same sample was measured repeatedly
- The statistical test(s) used AND whether they are one- or two-sided
Only common tests should be described solely by name; describe more complex techniques in the Methods section.
- A description of all covariates tested
- A description of any assumptions or corrections, such as tests of normality and adjustment for multiple comparisons
- A full description of the statistical parameters including central tendency (e.g. means) or other basic estimates (e.g. regression coefficient) AND variation (e.g. standard deviation) or associated estimates of uncertainty (e.g. confidence intervals)
- For null hypothesis testing, the test statistic (e.g. F , t , r) with confidence intervals, effect sizes, degrees of freedom and P value noted
Give P values as exact values whenever suitable.
- For Bayesian analysis, information on the choice of priors and Markov chain Monte Carlo settings
- For hierarchical and complex designs, identification of the appropriate level for tests and full reporting of outcomes
- Estimates of effect sizes (e.g. Cohen's d , Pearson's r), indicating how they were calculated

Our web collection on [statistics for biologists](#) contains articles on many of the points above.

Software and code

Policy information about [availability of computer code](#)

Data collection

Electrophysiology data were collected by using pCLAMP 10.6 software (Axon Instruments). Photometry data were collected by a fiber photometry system (Inper Ltd., China). Western Blot data were collected by using ChemiDoc Touch Imaging System and ChemiDoc MP. qRT-PCR data were collected by using LightCycler 480. Behavioral data were collected via using Any-maze software (Stoelting). Images were obtained by Nikon NIS Element 4.51 software, Olympus Slideview VS200 microscope and an Olympus Fluoview FV3000 confocal microscope. For bulk RNA-seq, StringTie(v1.3.4d) and ballgown(<http://www.bioconductor.org/packages/release/bioc/html/ballgown.html>) were used to estimate the expression levels of all transcripts and determine mRNA expression abundance by calculating FPKM value; for scRNA-seq, post-processing and quality control were carried out by 10X Cell Ranger package (v1.2.0; 10X Genomics). For electron microscopy, Thermo Scientific Talos L120C Electron Microscopy was used; For immunoelectron microscopy, TEM (Tecnaï Spirit Bio-Twin) with an accelerating voltage of 120 kV, charged-couple device (CCD) camera (Gatan, 15081901W0832, Germany) was used

Data analysis

Sequencing data were analyzed using the OmicStudio tools at <https://www.omicstudio.cn/tool>. Slice electrophysiology data were analyzed using Clampfit 10.6 (Molecular Devices) and Mini Analysis Program (Synaptosoft Inc., NJ). Photometry data were analyzed by using a processing software (Inper Ltd., China) and MATLAB code (Thinker Tech Nanjing Biotech Co., Ltd.). qRT-PCR data were analyzed by Lightcycler 480 software version 1.5. Western blot data were analyzed by Image Lab v5.2. Behavioral data were analyzed via using Graphpad prism v8, immunohistochemistry data were analyzed by Fiji-Image J v1.54f, and STORM data were analyzed by Nikon NIS Element 4.51 software.

For manuscripts utilizing custom algorithms or software that are central to the research but not yet described in published literature, software must be made available to editors and reviewers. We strongly encourage code deposition in a community repository (e.g. GitHub). See the Nature Portfolio [guidelines for submitting code & software](#) for further information.

Data

Policy information about [availability of data](#)

All manuscripts must include a [data availability statement](#). This statement should provide the following information, where applicable:

- Accession codes, unique identifiers, or web links for publicly available datasets
- A description of any restrictions on data availability
- For clinical datasets or third party data, please ensure that the statement adheres to our [policy](#)

All raw and processed sequencing data generated in this study have been deposited in the NCBI Gene Expression Omnibus (GEO) under accession numbers GSE287175 (bulk RNA-seq) and GSE287308 (scRNA-seq). Raw, uncropped images of western blots are provided in the Supplementary Information. Source data are provided with this paper.

Research involving human participants, their data, or biological material

Policy information about studies with [human participants or human data](#). See also policy information about [sex, gender \(identity/presentation\), and sexual orientation](#) and [race, ethnicity and racism](#).

Reporting on sex and gender	<input type="text" value="none"/>
Reporting on race, ethnicity, or other socially relevant groupings	<input type="text" value="none"/>
Population characteristics	<input type="text" value="none"/>
Recruitment	<input type="text" value="none"/>
Ethics oversight	<input type="text" value="none"/>

Note that full information on the approval of the study protocol must also be provided in the manuscript.

Field-specific reporting

Please select the one below that is the best fit for your research. If you are not sure, read the appropriate sections before making your selection.

- Life sciences Behavioural & social sciences Ecological, evolutionary & environmental sciences

For a reference copy of the document with all sections, see [nature.com/documents/nr-reporting-summary-flat.pdf](https://www.nature.com/documents/nr-reporting-summary-flat.pdf)

Life sciences study design

All studies must disclose on these points even when the disclosure is negative.

Sample size	<input type="text" value="The required sample sizes were determined based on our prior experience conducting similar experiments."/>
Data exclusions	<input type="text" value="Data points were excluded from analyses if the viral injection site or drug delivery site was out of the interested region."/>
Replication	<input type="text" value="All experiments were conducted using at least 2 cohorts of animals. The results were reproducible across cohorts and combined for the final analysis."/>
Randomization	<input type="text" value="For all experiments, mice were randomly grouped."/>
Blinding	<input type="text" value="For all experiments, investigators were blinded to group allocation during experimentation and data analysis. The offline data analysis was performed blindly."/>

Reporting for specific materials, systems and methods

We require information from authors about some types of materials, experimental systems and methods used in many studies. Here, indicate whether each material, system or method listed is relevant to your study. If you are not sure if a list item applies to your research, read the appropriate section before selecting a response.

Materials & experimental systems

Methods

n/a	Involved in the study
<input type="checkbox"/>	<input checked="" type="checkbox"/> Antibodies
<input checked="" type="checkbox"/>	<input type="checkbox"/> Eukaryotic cell lines
<input checked="" type="checkbox"/>	<input type="checkbox"/> Palaeontology and archaeology
<input type="checkbox"/>	<input checked="" type="checkbox"/> Animals and other organisms
<input checked="" type="checkbox"/>	<input type="checkbox"/> Clinical data
<input checked="" type="checkbox"/>	<input type="checkbox"/> Dual use research of concern
<input checked="" type="checkbox"/>	<input type="checkbox"/> Plants

n/a	Involved in the study
<input checked="" type="checkbox"/>	<input type="checkbox"/> ChIP-seq
<input checked="" type="checkbox"/>	<input type="checkbox"/> Flow cytometry
<input checked="" type="checkbox"/>	<input type="checkbox"/> MRI-based neuroimaging

Antibodies

Antibodies used

Primary antibodies: for western blot, rabbit anti-p62 (1:2000, #PM045, MBL), rabbit anti-Beclin-1(1:1000, #3495, CST), mouse anti-Atg7 (1:1000, #67341-1-Ig, Proteintech), mouse anti-ubiquitin (1:1000, #3936, CST), rabbit anti-p-AMPK α (Thr172) (1:1000, #2535, CST), rabbit anti-p-mTOR (1:1000, #ab137133, Abcam), rabbit anti-p-p70 S6 Kinase 1-T421/S424 (1:1000, #AP0502, Abclonal), rabbit anti-p-Akt (1:1000, #4058, CST), rabbit anti-Cleaved Caspase-3 (1:1000, #9664, CST), rabbit anti-GluA1 (1:1000, #ab31232, Abcam), rabbit anti-GluA2 (1:1000, #11994-1-AP, Proteintech), rabbit anti-GluN1 (1:1000, #ab109182, Abcam), rabbit Anti-GABAA Receptor alpha 1 (1:1000, #ab252430, Abcam), mouse anti- β -actin (1:5000, #MA5-15739, Thermo Fisher Scientific), or rabbit anti- α -tubulin (1:2000, #11224-1-AP, Proteintech); for immunohistochemistry experiment: mouse anti-LC3, 1:200, #A17424, Abclonal; rabbit anti-NeuN, 1:500, #A19086, Abclonal; rabbit anti-LC3, 1:1000, #ab192890, Abcam; mouse anti-PSD95, 1:500, #ab13552, Abcam; or guinea pig anti-NeuN, 1:500, #ABN90, Sigma-Aldrich; mouse anti-LC3, 1:100, #83506, CST. Secondary antibodies, for western blot, including anti-mouse IgG, HRP-linked antibody (1:10000, #31430, Thermo Fisher Scientific) and anti-rabbit IgG, HRP-linked antibody (1:5000, #31460, Thermo Fisher Scientific); goat anti-mouse, 1:100, #AS008, Abclonal or 1:1000, #A-21235, Thermo Fisher Scientific; goat anti-rabbit, 1:1000, #AS060, Abclonal, or 1:1000, #A-11008, Thermo Fisher Scientific; goat anti-guinea pig, 1:1000, #A-21435, Thermo Fisher Scientific; goat anti-mouse, 1:1,000, #A11001, Invitrogen.

Validation

Here are the links of the websites that show validation of the antibodies used in this study:

Primary antibodies:

Western blot:

<https://ruo.mbl.co.jp/bio/e/dtl/A/?pcd=PM045>

https://www.cellsignal.com/products/primary-antibodies/beclin-1-d40c5-rabbit-mab/3495?qs=keyword_redirect&qt#3495

<https://www.ptglab.com/products/ATG7-Antibody-67341-1-Ig.htm>

<https://www.cellsignal.com/products/primary-antibodies/ubiquitin-p4d1-mouse-mab/3936>

<https://www.cellsignal.com/products/primary-antibodies/phospho-ampka-thr172-40h9-rabbit-mab/2535>

<https://www.abcam.cn/products/primary-antibodies/mtor-phospho-s2481-antibody-epr427n-ab137133.html>

<https://abclonal.com.cn/catalog/AP0502>

<https://www.cellsignal.com/products/primary-antibodies/phospho-akt-ser473-193h12-rabbit-mab/4058>

<https://www.cellsignal.com/products/primary-antibodies/cleaved-caspase-3-asp175-5a1e-rabbit-mab/9664>

<https://www.abcam.cn/products/primary-antibodies/glutamate-receptor-1-ampa-subtype-antibody-ab31232.html>

<https://www.ptglab.com/products/GRIA2-Antibody-11994-1-AP.htm>

<https://www.abcam.cn/products/primary-antibodies/nmdar1-antibody-epr24812-ab109182.html>

<https://www.abcam.cn/products/primary-antibodies/gaba-a-receptor-alpha-1-antibody-epr23539-255-ab252430.html>

<https://www.thermofisher.cn/cn/zh/antibody/product/Beta-Actin-Loading-Control-Antibody-clone-BA3R-Monoclonal/MA5-15739-BTIN>

<https://www.ptglab.com/products/TUBA1B-Antibody-11224-1-AP.htm>

Immunohistochemistry:

<https://abclonal.com.cn/catalog/A17424>

<https://abclonal.com.cn/catalog/A19086>

<https://www.abcam.cn/products/primary-antibodies/lc3b-antibody-epr18709-autophagosome-marker-ab192890.html>

<https://www.abcam.cn/products/primary-antibodies/psd95-antibody-7e3-1b8-synaptic-marker-ab13552.html>

<https://www.sigmaaldrich.cn/CN/zh/product/mm/abn90>

<https://www.cellsignal.com/products/primary-antibodies/lc3b-e5q2k-mouse-mab/83506>

Secondary antibodies:

western blot:

<https://www.thermofisher.cn/cn/zh/antibody/product/Goat-anti-Mouse-IgG-H-L-Secondary-Antibody-Polyclonal/31430>

<https://www.thermofisher.cn/cn/zh/antibody/product/Goat-anti-Rabbit-IgG-H-L-Secondary-Antibody-Polyclonal/31460>

<https://abclonal.com.cn/catalog/AS008>

<https://www.thermofisher.cn/cn/zh/antibody/product/Goat-anti-Mouse-IgG-H-L-Cross-Adsorbed-Secondary-Antibody-Polyclonal/A-21235>

<https://abclonal.com.cn/catalog/AS060>

<https://www.thermofisher.cn/cn/zh/antibody/product/Goat-anti-Rabbit-IgG-H-L-Cross-Adsorbed-Secondary-Antibody-Polyclonal/A-11008>

<https://www.thermofisher.cn/cn/zh/antibody/product/Goat-anti-Guinea-Pig-IgG-H-L-Highly-Cross-Adsorbed-Secondary-Antibody-Polyclonal/A-21435>

<https://www.thermofisher.cn/cn/zh/antibody/product/Goat-anti-Mouse-IgG-H-L-Cross-Adsorbed-Secondary-Antibody-Polyclonal/A-11001>

Animals and other research organisms

Policy information about [studies involving animals](#); [ARRIVE guidelines](#) recommended for reporting animal research, and [Sex and Gender in Research](#)

Laboratory animals	All mice (aged 7-15 weeks, if not specified) were bred in our colony (i.e., Atg7flox/ flox lines50 and GFP-LC3 lines) or purchased from SLAC (i.e., C57BL/6J and CD-1 mice). CD-1 mice (4-6 months old retired breeder) were single-housed, and all other mice were housed 4-5 per cage if not specified. All animals were subjected to a 12-hour light-dark cycle (light on from 7 a.m. to 7 p.m.) with food and water ad libitum. All mice were housed in a stable environment (23-25 °C ambient temperature and 50% humidity).
Wild animals	This study did not involve wild animals.
Reporting on sex	Only male mice were used in this study.
Field-collected samples	No field-collected samples were applied in this study.
Ethics oversight	All animal research and experimental procedures were approved by the Animal Care and Use Committee of the animal facility at Zhejiang University.

Note that full information on the approval of the study protocol must also be provided in the manuscript.

Plants

Seed stocks	N/A
Novel plant genotypes	N/A
Authentication	N/A